Prioritized multi-objective optimization of a sandwich panel

Jean-Antoine Desideri, Pierre Leite, Quentin Mercier

To cite this version:

Jean-Antoine Desideri, Pierre Leite, Quentin Mercier. Prioritized multi-objective optimization of a sandwich panel. [Research Report] RR-9362, INRIA Sophia Antipolis - Méditerranée (France). 2020. hal-02931770

HAL Id: hal-02931770

https://inria.hal.science/hal-02931770

Submitted on 7 Sep 2020

Prioritized multi-objective optimization of a sandwich panel

Jean-Antoine Désidéri, Pierre Leite , Quentin Mercier

RESEARCH REPORT

N° 9362

September 8, 2020

Project-Team Acumes

ISSN 0249-6399 ISRN INRIA/RR--9362--FR+ENG

Prioritized multi-objective optimization of a sandwich panel

Jean-Antoine Désidéri*, Pierre Leite †, Quentin Mercier ‡

Project-Team Acumes

Research Report n° 9362 — September 8, 2020 — 37 pages

Abstract: This report is intended to demonstrate numerically the potential of the prioritized multi-objective optimization approach by applying it to the sizing of a sandwich panel with respect to mechanical criteria: mass, critical failure forces under bending load (1st and 2nd modes), and blast mitigation measured by the core energy absorption, deflection, or both. Several objective functions are defined based on analytical models. Four numerical test-cases are documented. In each test-case, the Pareto front associated with two constrained criteria only, including mass, is first established; then, the design is improved by accounting for one or two additional criteria by the construction of a continuum of Nash equilibria tangent to the front in function space at the starting point.

Key-words: differentiable multi-objective optimization, criterion prioritization, Nash game

---

[*] Inria Research Director, emeritus

[†] R & D Project Manager, Essilor, Créteil (France)

[‡] Formerly at Onera Châtillon (France)

RESEARCH CENTRE
SOPHIA ANTIPOLIS – MÉDITERRANÉE

2004 route des Lucioles - BP 93
06902 Sophia Antipolis Cedex

Optimisation multiobjectif hiérarchisée d'un panneau sandwich

Résumé : Ce rapport a pour objectif de faire la démonstration numérique de l'approche d'optimisation multiobjectif hiérarchisée en l'appliquant au dimensionnement d'un panneau sandwich vis-à-vis de critères mécaniques: masse, forces critiques de défaillance sous charge de flexion (1er et 2ème modes), et résistance à une explosion mesurée par l'absorption d'énergie par le cœur, la déflexion au centre, ou les deux. Plusieurs fonctions objectifs sont définies à partir de modèles analytiques. Quatre cas-tests sont documentés. Pour chaque cas-test, le front de Pareto associé à deux critères seulement, sous contrainte, dont la masse, est d'abord établi; puis, la conception est améliorée par la prise en compte d'un ou deux critères additionnels par la construction d'un continuum d'équilibres de Nash tangent dans l'espace des fonctions au front au point de départ.

Mots-clés : optimisation multiobjectif différentiable, hiérachisation des critères, jeu de Nash

1 Introduction

In his thesis [7], P. Leite has described and tested a variety of practical models potentially significant to devise sandwich materials and optimize their structural performance. The thesis contains numerous design optimization case studies conducted using a genetic algorithm.

Q. Mercier in his thesis [8], and related works [11] [12] [9] [10], has developed a stochastic descent method and tested the potential of his algorithm to handle various types of difficulties a gradient-based optimization algorithm can be subject to: uncertainties, non differentiabilty, non convexity. The main application tests were carried out for the design and reliability of a sandwich plate, based on the models described by P. Leite.

The report is aimed at illustrating the efficacy of a prioritized approach [4] in a multi-objective optimization numerical experiment involving more than two criteria. To serve this purpose, the same type of structural element subject to some of these models, in a deterministic context, is used to define criteria in relation with

- mass;
- critical failure forces associated with bending loads (1st and 2nd modes);
- blast mitigation by increasing the blast energy absorption, or reducing the deflection at the center of the element.

2 Geometry to be optimized

2.1 Description

The structural element under consideration is a three-layer sandwich aluminum panel depicted in Figure 1. The thicknesses of the upper and lower layers and core are respectively $\mathbf{t}_u$, $\mathbf{t}_l$ and $\mathbf{t}_c$. The following dimensions are used throughout $b = 5$ cm, $\ell = 50$ cm.

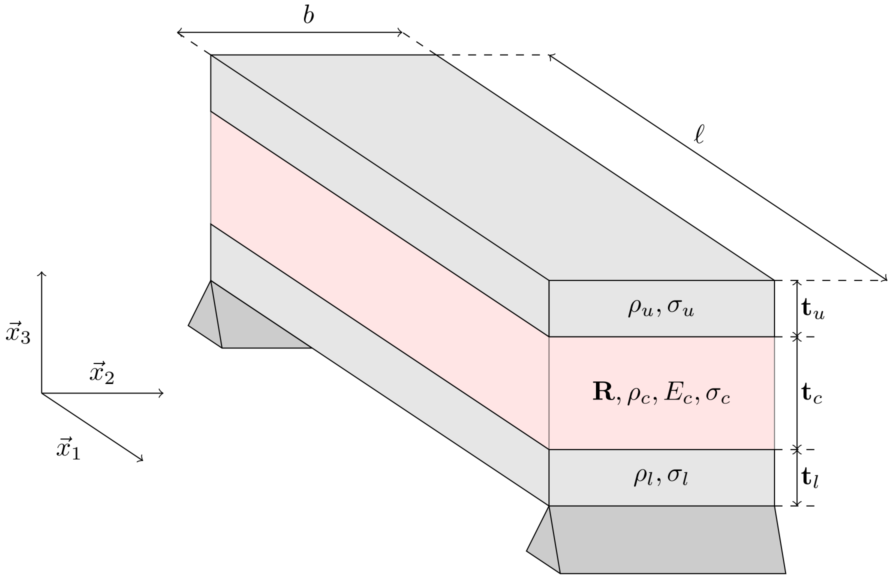

Figure 1: Geometry of the sandwich panel

The core is made of honeycomb foam. Such structural elements are widely used by industrial manufacturers for their exceptional mechanical properties. Illustrations can be found in many engineering sites. One such illustration is provided in Figure 2.

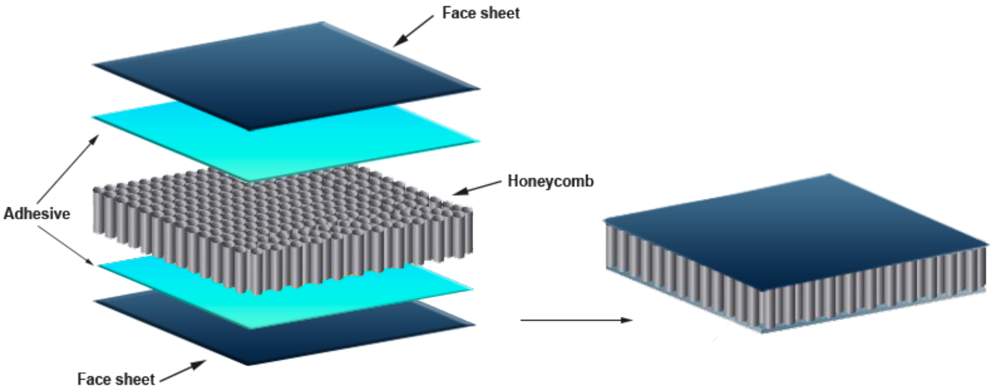

Figure 2: Illustration of a typical element with honeycomb core

In the present case, the honeycomb is symmetrical and its dimensions are defined Figure 3.

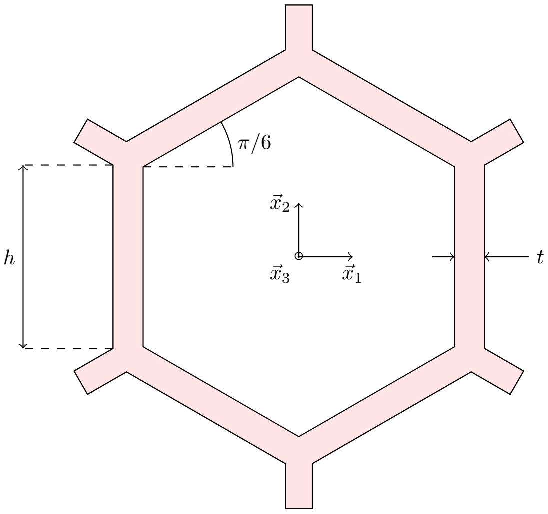

Figure 3: Dimensions of honeycomb core

In summary, the thicknesses $\mathbf{t}_u$, $\mathbf{t}_l$ and $\mathbf{t}_c$, as well as the ratio $\mathbf{R} = t/h$ of thickness to length of the honeycomb cell walls (see Figure 3) constitute the design optimization variables.

2.2 Constraints

Expressing all sizes in meters, the design variables are subject to the following interval constraints

$$\mathbf{t}_u,\ \mathbf{t}_l \in [0.03, 0.14], \quad \mathbf{t}_c \in [0.05, 0.19], \quad \mathbf{R} \in [0.01, 0.20], \tag{1}$$

and the total thickness to the following bound:

$$e = \mathbf{t}_u + \mathbf{t}_l + \mathbf{t}_c \leq 0.25. \tag{2}$$

3 Parameterization

In order to satisfy the interval constraints automatically, the following change of variables is adopted:

$$\begin{aligned}\mathbf{t}_u &= 0.085 + 0.055 \sin x_1\\ \mathbf{t}_b &= 0.085 + 0.055 \sin x_2\\ \mathbf{t}_c &= 0.120 + 0.070 \sin x_3\\ \mathbf{R} &= 0.105 + 0.095 \sin x_4.\end{aligned}$$

where the variables x_i's are initially set in the interval $[-\pi/2, \pi/2]$ but may not remain in it in the course of the optimization.

Besides, in order to satisfy the bound constraint on the total thickness, an additional variable is introduced, x_5, as a slack variable, and the constraint is transformed into the following equality constraint:

$$c_1(\mathbf{x}) = 0.29 + 0.055\left(\sin x_1 + \sin x_2\right) + 0.070 \sin x_3 - 0.25 + x_5^2 = 0. \tag{3}$$

In this way, the problem involves 5 variables, and 1 constraint of equality type.

4 Mechanical characteristics and physical criteria

4.1 Mass

For the upper and lower skins, density and elastic limit are given by

$$\rho_u = \rho_l = \rho = 2700 \text{ kg/m}^3, \quad \sigma_u = \sigma_l = \sigma = 250 \text{ MPa}. \tag{4}$$

Concerning the honeycomb core, Gibson and Ashby [6] have established the following characteristics of an equivalent plate:

$$\rho_c = \frac{2\mathbf{R}}{\sqrt{3}}\rho, \quad \sigma_c = 5.6\mathbf{R}^{\frac{5}{3}}\sigma. \tag{5}$$

Based on the geometrical elements and this equivalence, the element mass (per unit area of outer/lower surface) is

$$m = \rho_u \mathbf{t}_u + \rho_c \mathbf{t}_c + \rho_l \mathbf{t}_l. \tag{6}$$

As usual, mass is to be minimized.

Mass-related dimensionless cost function, $\varphi_m(\mathbf{x})$

$$\varphi_m(\mathbf{x}) = \frac{m}{\overline{m}} \tag{7}$$

where $\overline{m}$ is an average value of mass set from the interval constraints,

$$\overline{m} = \overline{\rho_u}\,\overline{\mathbf{t}_u} + \overline{\rho_{\mathbf{R}}}\,\overline{\mathbf{t}_c} + \overline{\rho_b}\,\overline{\mathbf{t}_b} = \rho\left(\overline{\mathbf{t}_u} + \overline{\mathbf{t}_b}\right) + \frac{2\overline{\mathbf{R}}}{\sqrt{3}}\rho\overline{\mathbf{t}_c}. \tag{8}$$

where barred quantities are average values. This gives

$$\begin{aligned}\varphi_m(\mathbf{x}) &= \frac{0.170 + 0.055(\sin x_1 + \sin x_2) + (0.120 + 0.070 \sin x_3)\,\frac{2\mathbf{R}}{\sqrt{3}}}{\tau}\\ &= \frac{0.170 + 0.055(\sin x_1 + \sin x_2) + (0.120 + 0.070 \sin x_3)\,\dfrac{0.21 + 0.19 \sin x_4}{\sqrt{3}}}{\tau}\end{aligned} \tag{9}$$

where $\tau = \overline{m}/\rho = 0.170 + \frac{2}{\sqrt{3}} \times 0.120 \times 0.105 \doteq 0.1845$ m.

4.2 Flexural critical forces

Following [7] (Section 2.2) and [1], the first two modes of failure in flexion are core indentation and exceeded lower-skin elastic resistance, depicted in Figure 4.

a) Core indentation

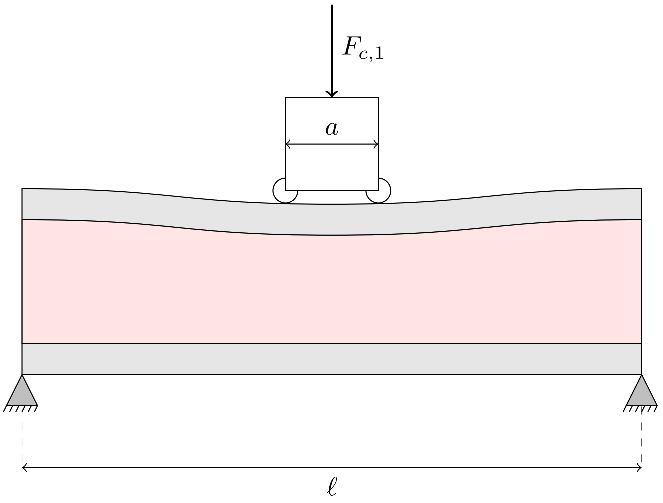

b) Exceeded lower-skin elastic resistance

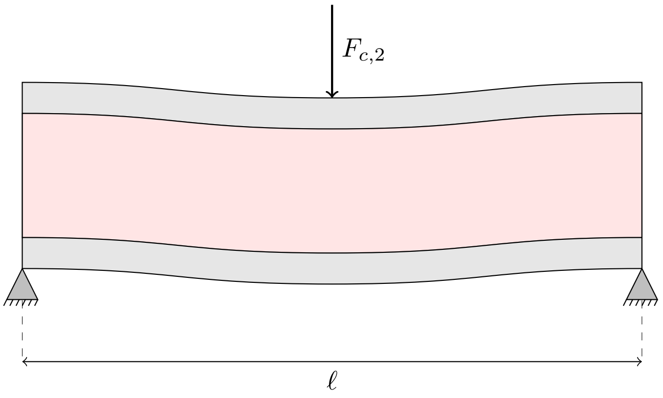

Figure 4: First two modes of failure in flexion

These modes are triggered under the following critical forces:

$$\begin{cases} F_{c,1} & = 2b\mathbf{t}_u\sqrt{\sigma_c\sigma_u} + ab\sigma_c \\ F_{c,2} & = \dfrac{4}{\ell}b\mathbf{t}_l\left(\mathbf{t}_c + \dfrac{\mathbf{t}_u + \mathbf{t}_l}{2}\right)\sigma_l. \end{cases} \tag{10}$$

We have used the following constant $a = 0.01$ m.

The critical forces are to be maximized to minimize the risk of failure according to these modes.

Cost functions related to the critical flexural forces, φ_1 and φ_2

$$\begin{cases} \varphi_1(\mathbf{x}) & = \dfrac{ab\sigma}{F_{c,1}} = \dfrac{1}{2}\dfrac{\mathbf{t}_u}{a}\sqrt{\dfrac{\sigma_c}{\sigma}} + \dfrac{\sigma_c}{\sigma} \\ \varphi_2(\mathbf{x}) & = \dfrac{ab\sigma}{F_{c,2}} = \dfrac{a\ell}{4\mathbf{t}_l\left(\mathbf{t}_c + \dfrac{\mathbf{t}_u + \mathbf{t}_l}{2}\right)} \end{cases} \tag{11}$$

4.3 Blast mitigation

This subsection follows closely the model provided in [7] (Section 2.5) which was an adaptation of the model by Fleck and Deshpande [5], also discussed in [13].

There, the effect of the blast has been described as a three-stage phenomenon.

The first stage of the blast is considered as a one-dimensional fluid-structure interaction. Given the peak pressure p_0 and the duration θ, the maximum achievable impulse I is given by:

$$I = \int_0^\infty 2p_0 e^{-t/\theta} dt = 2p_0\theta \tag{12}$$

and the ratio between this maximum impulse and the impulse conveyed to the upper face, I_{trans}, is:

$$\frac{I_{\text{trans}}}{I} = \psi^{-\frac{\psi}{\psi-1}} \tag{13}$$

where

$$\psi = \frac{\rho_w c_w \theta}{m_u} \tag{14}$$

is dimensionless. Here, $m_u = \rho_u \mathbf{t}_u$ is the upper face mass (per unit area), ρ_w and c_w are the fluid density and wave velocity. The following data have been used: $\rho_w = 51.24$ kg/m^3, $c_w = 330$ m/s, $\theta = 0.1$ ms, and $p_0 = 50$ MPa.

It is assumed that the upper face undergoes an acceleration to the velocity

$$v_0 = \frac{I_{\text{trans}}}{m_u}. \tag{15}$$

Stage II relates to core crushing. The upper face decelerates from v_0 to v_f given by the expression of conservation of momentum:

$$(m_u + m_c + m_l)v_f = m_u v_0 \tag{16}$$

so that

$$\frac{v_f}{v_0} = \frac{m_u}{m_u + m_c + m_l} = \frac{\mathbf{t}_u}{\mathbf{t}_u + \mathbf{t}_l + \frac{\rho_c}{\rho}\mathbf{t}_c}. \tag{17}$$

During this stage, an energy U_{lost} is dissipated, and the energy balance writes:

$$\tfrac{1}{2} m_u v_0^2 = U_{\text{lost}} + \tfrac{1}{2}(m_u + m_c + m_l)v_f^2 \tag{18}$$

(energies per unit area) and this provides

$$\frac{U_{\text{lost}}}{v_0^2} = \frac{m_u(m_c + m_l)}{2(m_u + m_c + m_l)} = \frac{t_u\left(t_l + \frac{\rho_c}{\rho}t_c\right)}{2\left(t_u + t_l + \frac{\rho_c}{\rho}t_c\right)}. \tag{19}$$

The quantity U_{lost} measures the energy absorbed by the core and should be as large as possible. It is assumed that the energy loss results from plastic dissipation during the core compression so that:

$$U_{\text{lost}} = \sigma_c \varepsilon_c \mathbf{t}_c \tag{20}$$

and this provides

$$\varepsilon_c = U_{\text{lost}}/(\sigma_c \mathbf{t}_c) \tag{21}$$

Additionally, ε_c must be limited to the densification strain

$$\varepsilon_D = 1 - 1.4\frac{\rho_c}{\rho} = 1 - \frac{2.8}{\sqrt{3}}\mathbf{R}. \tag{22}$$

At the end of Stage II, the sandwich beam has a uniform velocity v_f. Stage III corresponds to the dissipation of the remaining kinetic energy by bending and stretching of the beam. The analysis proposed in [7] divides the phenomenon into two phases. During the first phase, a central portion of the beam translates at a velocity v_f while a segment of length ξ rotates symmetrically at the supports. Thus the bending moment M varies from M_0 at the support to $-M_0$ at the end of the rotating segment, and is constant in the central portion.

The first phase ends when $\xi = L = \ell/2$ at time $t = T_1$:

$$T_1 = \frac{M_0}{N_0 v_f}\left(\sqrt{4 + \frac{mL^2 v_f^2 N_0}{3M_0^2}} - 2\right) \tag{23}$$

where m is the total mass per unit length, given in (6). The central deflection is thus:

$$w_1 = v_f T_1 = \frac{M_0}{N_0}\left(\sqrt{4 + \frac{mL^2 v_f^2 N_0}{3M_0^2}} - 2\right) \tag{24}$$

where N_0 is the longitudinal force.

During the second phase, plastic hinges occur at the supports and at the mid-span, and the velocity profile is assumed to be triangular. The central deflection of the sandwich beam w is given by:

$$w = \sqrt{\frac{v_f^2}{\omega^2} + \left(\frac{2M_0}{N_0} + w_1\right)^2} - \frac{2M_0}{N_0} \tag{25}$$

where $\omega = \sqrt{3N_0/m}/L$ is a contant in s^{-1}.

In the above, the longitudinal force is expressed as follows:

$$N_0 = \sigma(\mathbf{t}_u + \mathbf{t}_l) + \sigma_c \mathbf{t}_c = \sigma\left(\mathbf{t}_u + \mathbf{t}_l + \frac{\sigma_c}{\sigma}\mathbf{t}_c\right) \tag{26}$$

and the bending moment as follows:

$$M_0 = \sigma(e_u \mathbf{t}_u + e_l \mathbf{t}_l) + \sigma_c\left(\frac{c_u^2}{2} + \frac{c_l^2}{2}\right) = \sigma\left[e_u \mathbf{t}_u + e_l \mathbf{t}_l + \frac{\sigma_c}{\sigma}\left(\frac{c_u^2}{2} + \frac{c_l^2}{2}\right)\right] \tag{27}$$

in which e_u (resp. e_l) is the distance between the centroid of the upper (resp. lower) face and the neutral axis,

$$e_u = c_u + \tfrac{1}{2}\mathbf{t}_u, \quad e_l = c_l + \tfrac{1}{2}\mathbf{t}_l, \tag{28}$$

and:

$$c_u = \tfrac{1}{2}(1 - \varepsilon_c)\frac{\mathbf{t}_l - \mathbf{t}_u + \mathbf{t}_c}{\rho_c/\rho}, \quad c_l = \tfrac{1}{2}(1 - \varepsilon_c)\frac{\mathbf{t}_u - \mathbf{t}_l + \mathbf{t}_c}{\rho_c/\rho}. \tag{29}$$

In conclusion, blast mitigation can be achieved by minimizing the central deflection w of (25).

Cost functions related to blast mitigation, φ_u and φ_w Two such cost functions are defined dimensionless. The first is related to the core energy absorption

$$\varphi_u(\mathbf{x}) = \frac{\rho_w c_w^3 \theta}{U_{\text{lost}}}. \tag{30}$$

The second is the dimensionless deflection:

$$\varphi_w = \frac{w}{\ell}. \tag{31}$$

5 Definition of test-cases, prioritized-optimization procedure and presentation of the results

Four test-cases have been considered from TC_1 to TC_4. Each test-case involves either 3 or 4 objective functions $\{f_j\}$ defined from the physical cost functions φ_m (mass), φ_1 and φ_2 (related to critical flexural forces), φ_u (related to the core energy absorption under blast), and φ_w (element deflection under blast). The optimization variables are the 5 components of vector $\mathbf{x}$. All test-cases are subject to the constraint (3). Table 1 indicates the definition of the objective functions in the four test-cases. A distinction is made between primary and secondary objective functions.

Test-case	f_1 (primary)	f_2 (primary)	f_3 (2ndary)	f_4 (2ndary)
TC_1	φ_m	φ_1	φ_2	-
TC_2	φ_m	$\frac{1}{2}(\varphi_1+\varphi_2)$	$\frac{1}{2}e^{\varphi_u}$	-
TC_3	φ_m	$\frac{1}{2}(\varphi_1+\varphi_2)$	φ_w	-
TC_4	φ_m	$\frac{1}{2}(\varphi_1+\varphi_2)$	φ_w	$\frac{1}{2}e^{\varphi_u}$

Table 1: Definition of test-cases

In all numerical experiments, the prioritized optimization approach proceeds in two phases.

The first phase of optimization consists in identifying the Pareto front associated with the sole primary objective functions (f_1, f_2) under the constraint $c_1(\mathbf{x}) = 0$.

For this, a discretization of the admissible domain in R^5 is first set up. The variables x_1, x_2 and x_3 are discretized by step of $\frac{1}{10}$. Only the triplets for which the constraint on thickness, (3), can be solved for the slack variable x_5 are retained, and this results in 307 points, each of which yields 10 points in the admissible domain by similar discretization of x_4. In total, this produces 3070 admissible points.

This first phase of optimization has been performed using the software platform [2] under the heading "Solving a constrained problem". Each admissible point serves as a starting point to the Quasi-Riemannian Multiple-Gradient Descent Algorithm (QR-MGDA [2]-[3]). These independent iterations produce 3070 limiting points. Since the same setting of the numerical method has been adopted in all 3070 cases handled in a single run, some of these limiting points show a lesser degree of convergence to the Pareto front, due to the slightly inadequate global setting of the method parameters. Thus, only the non-dominated points are retained. Nevertheless, these latter are in great number, about 1000, in both cases (934 in the TC_1 setting; 1170 in the TC_2-TC_3-TC_4 setting), and permit to define a very clear, convex and smooth Pareto front in (f_1, f_2) subject to $c_1(\mathbf{x}) = 0$.

The second phase of optimization consists in first electing a representative Pareto-optimal solution from the front, attained at say $\mathbf{x} = \mathbf{x}_A^\star$, and then constructing a continuum of Nash equilibria originating from $\mathbf{x}_A^\star$, tangent to the front in function space, and along which the secondary objective function f_3 is reduced, and f_4 as well in TC_4. This phase of optimization has been conducted using the software platform [2] under the heading "Solving a prioritized optimization problem". Two files are provided to define the execution of a test-case:

- `my_testcase.dat` in which a few method parameters are set, mostly title, dimensions and accuracy sizing parameters; this file is defined in Appendix A in all four cases;

- `my_functions.f` that contains the procedures defining the primary and secondary objective functions, and the constraints in Fortran 77 or 90;

see the web site for details.

The prioritized optimization approach may be viewed as a way to handle three objective functions, or more, by decoupling the treatment of the primary objective functions from the treatment of the secondary ones. One can also consider the entire process as a form of Stackelberg game in which the treatment of the secondary cost functions is subordinated to the quasi Pareto-optimality of the primary ones.

In each test-case, the results are illustrated in five figures. The first figure shows the

- Pareto front in (f_1, f_2), in magenta symbols, and secondary objective functions, f_3 or (f_3, f_4), using symbols of other colors, representing f_1 horizontally, and f_2, f_3 and possibly f_4 vertically, and the continuum of Nash equilibria in terms of (f_1, f_2), (f_1, f_3), and (f_1, f_4) (in TC_4), by solid lines respecting the color associated with the second function.

This figure concentrates results from both phases of optimization. The following four figures provide the

- Objective functions $\{f_j\}$ $(j = 1, 2, 3)$, and f_4 in the case of TC_4,
- Objective functions $\{f_j/f_j(\mathbf{x}_A^\star\}$ ($j = 1, 2, 3$, and 4 in TC_4) in proportion to their respective values at $\mathbf{x}_A^\star$,
- Optimization variables x_i $(i = 1, \dots, 5)$,
- Constraint function $c_1(\mathbf{x})$,

all evaluated along the continuum of Nash equilibria and expressed as functions of the continuation parameter ε.

6 Test-Case TC_1: Mass and critical flexural forces

The two primary and the single secondary objective functions were defined in the first row of Table 1. In this test-case, the first phase of optimization, conducted considering only mass and first mode of failure in flexion, has led to 934 non dominated designs. The critical flexural force associated with the second mode of failure was then evaluated for the Pareto-optimal design-points. Larger values of the objective function f_3 corresponding to a second-mode critical force inferior to the first, were found for the heavier designs (see blue symbols on Figure 5). Hence for such designs, the second failure mode would be triggered first.

Starting from such a design, the prioritized optimization procedure can be used to correct this deficiency, and in fact, to achieve a design for which both critical forces, $F_{c,1}$ and $F_{c,2}$, are equal to a value only slightly inferior to the original value of $F_{c,1}$.

As an example, the (f_1, f_2)-Pareto-optimal design point for which $f_1 \approx 0.3702$ was considered, and defined as the starting point $\mathbf{x}_A^\star$ to initiate the computation of the continuum of Nash equilibria conducted to reduce f_3 using the MGDA platform [2]. The graphics outputs corresponding to this experiment are given Figures 5 -6 -7 -8 -9. The Pareto front and continuum paths in function space are indicated on Figure 5. The continuum of Nash equilibria is represented by the yellow path ab in terms of (f_1, f_2) and the blue path a'b' in terms of (f_1, f_3). These paths intersect at a point i where $f_1 \approx 0.4111$ which corresponds to a mass increase of some 11%. Correspondingly, the first critical force diminishes of about 0.2%, the second critical force, inversely proportional to f_3, increases of more than 57%, and, at point i, they equate (see Table 2).

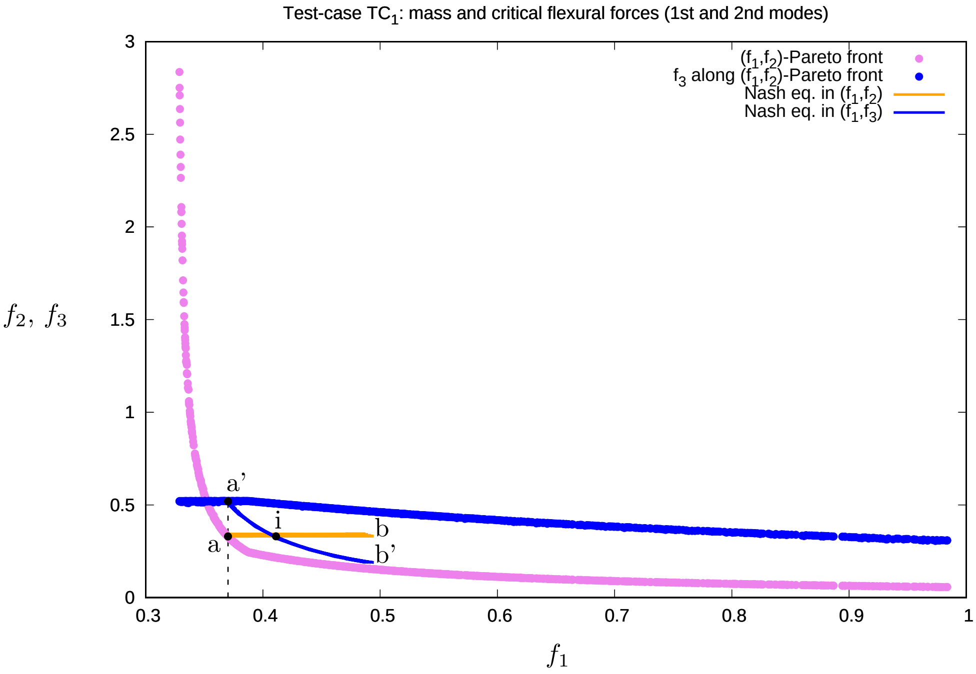

Figure 5: Test-case TC$_1$: Pareto front and continuum of Nash equilibria ($f_1 = \varphi_m,\ f_2 = \varphi_1,\ f_3 = \varphi_2$)

Test-case TC$_1$

ε	f_1	f_2	f_3
0.	0.3702	0.3297	0.5194
0.6298	0.4111	0.3304	0.3304
	(+11.1%)	(+0.2%)	(-36.4%)

Table 2: Values of the objective functions at start and at the interpolated intersection point

Other remarks

- Figures 6-7 are two representations of the variation of the objective functions along the continuum. At point i, $f_2 = f_3$, that is, $F_{c,1} = F_{c,2}$.
- Figure 8 indicates that the game mostly involves an exchange between x_3 and x_5, that is, the core thickness and the slack variable that permits to enforce the bound on total thickness. Thus, the game tends to make the element thicker up to the allowable limit.
- Figure 9 represents the variation with ε of the constraint function $c_1(\mathbf{x})$ along the continuum. Near the tail of the continuum, the process eventually becomes unstable. However, for the relevant part of the continuum, the constraint violation $|c_1(\mathbf{x})|$ remains below 10^{-5}, that is, clearly within the accuracy tolerance bound of 10^{-4}.

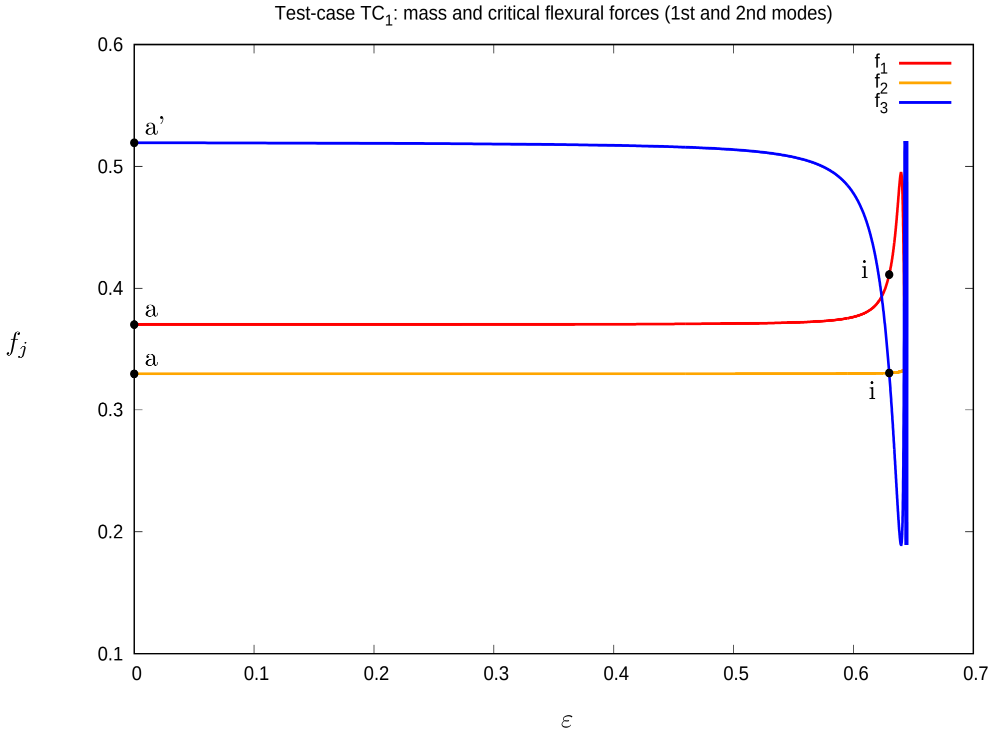

Figure 6: Test-case TC$_1$: Objective functions $\{f_j\}$ along the continuum as functions of the continuation parameter ε $(f_1 = \varphi_m,\ f_2 = \varphi_1,\ f_3 = \varphi_2)$

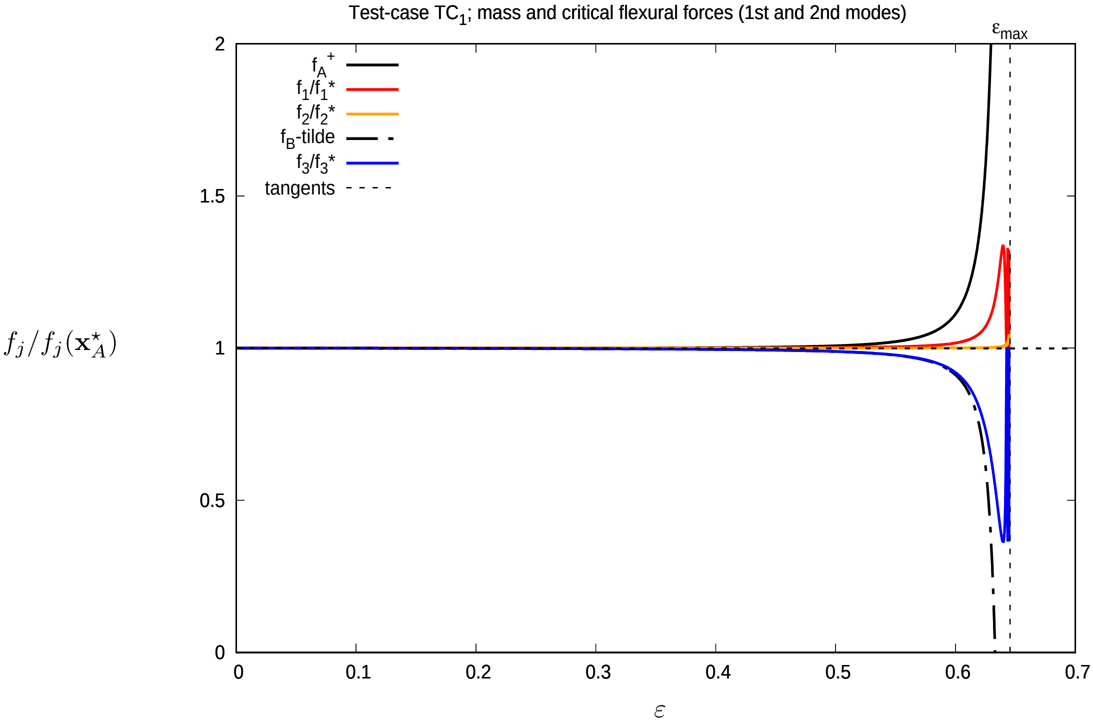

Figure 7: Test-case TC$_1$: Objective functions $\{f_j/f_j(\mathbf{x}_A^\star)\}$ along the continuum as functions of the continuation parameter ε $(f_1 = \varphi_m,\ f_2 = \varphi_1,\ f_3 = \varphi_2)$

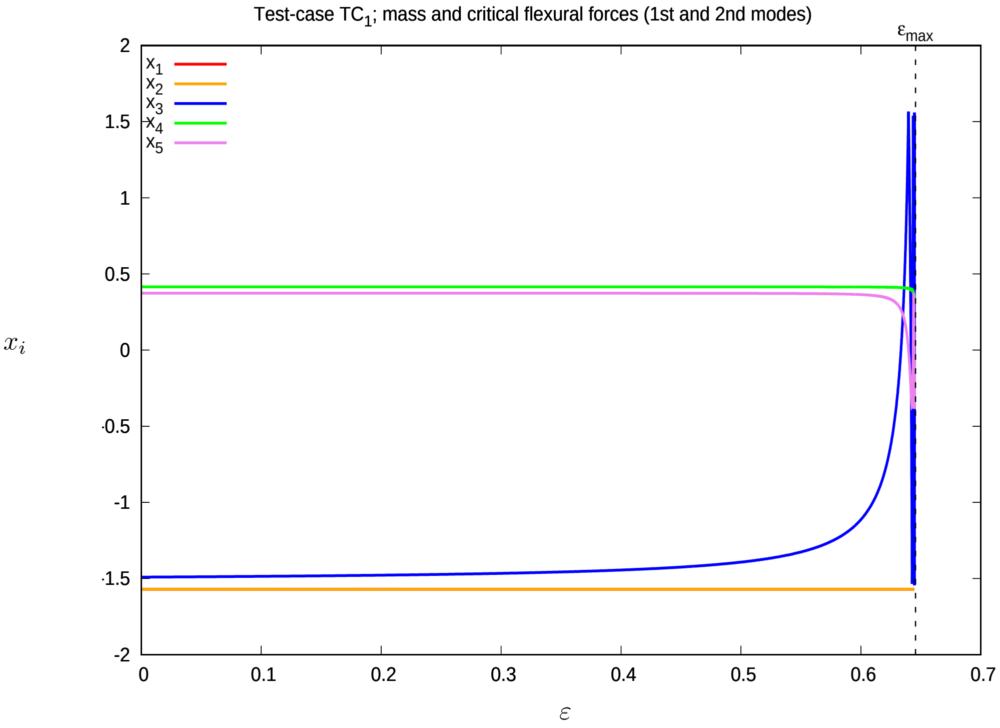

Figure 8: Test-case TC$_1$: Optimization variables $\{x_i\}$ along the continuum as functions of the continuation parameter ε $(f_1 = \varphi_m,\ f_2 = \varphi_1,\ f_3 = \varphi_2)$

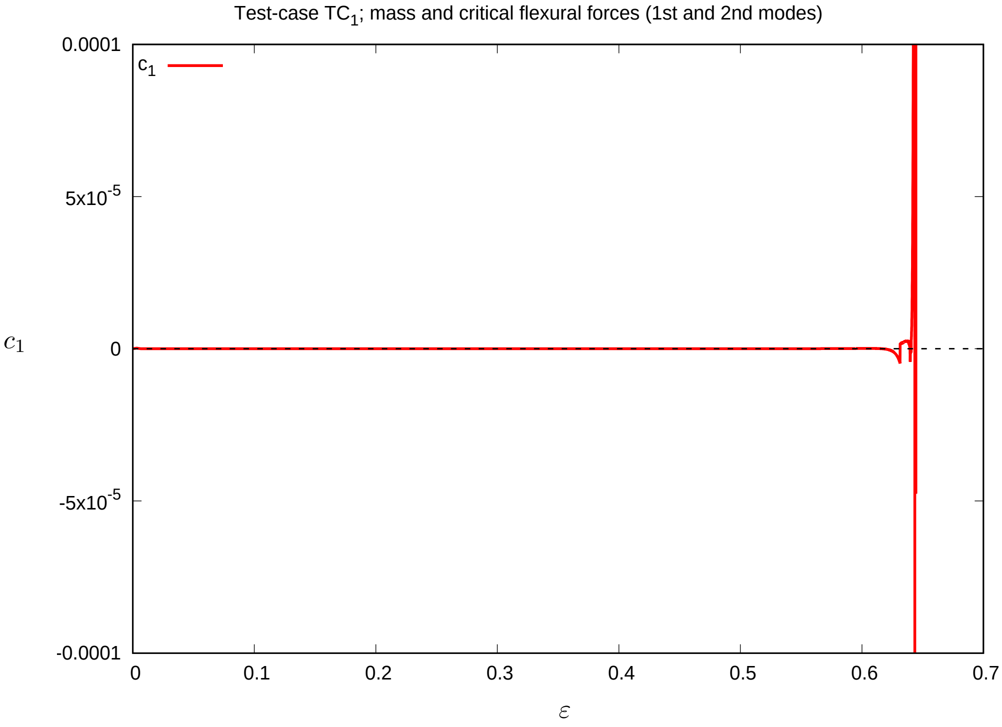

Figure 9: Test-case TC$_1$: Constraint function c_1 along the continuum as functions of the continuation parameter ε $(f_1 = \varphi_m,\ f_2 = \varphi_1,\ f_3 = \varphi_2)$

Conclusion

The treatment of Test-case TC$_1$ has permitted to demonstrate that with an acceptable increase in mass (+11%) and a very marginal reduction of first flexural force (<0.6%), the second flexural force was drastically increased (>56%) to equate the first. The satisfaction of the inequality constraint on thickness by the technique of the slack variable operates very well.

7 Test-case 2: Blast mitigation by augmenting the energy absorption by the core

In this test-case, we have used again mass as the first primary objective function, but a blend of the two critical flexural forces as the second, as indicated in the second row of Table 1. We proceeded as in Test-case 1 to determine first the (f_1, f_2)-Pareto front. Here 1170 non-dominated limiting points were retained from the 3070 convergence paths. The resulting front, given in Figure 10, is very similar: densely-defined, smooth and convex.

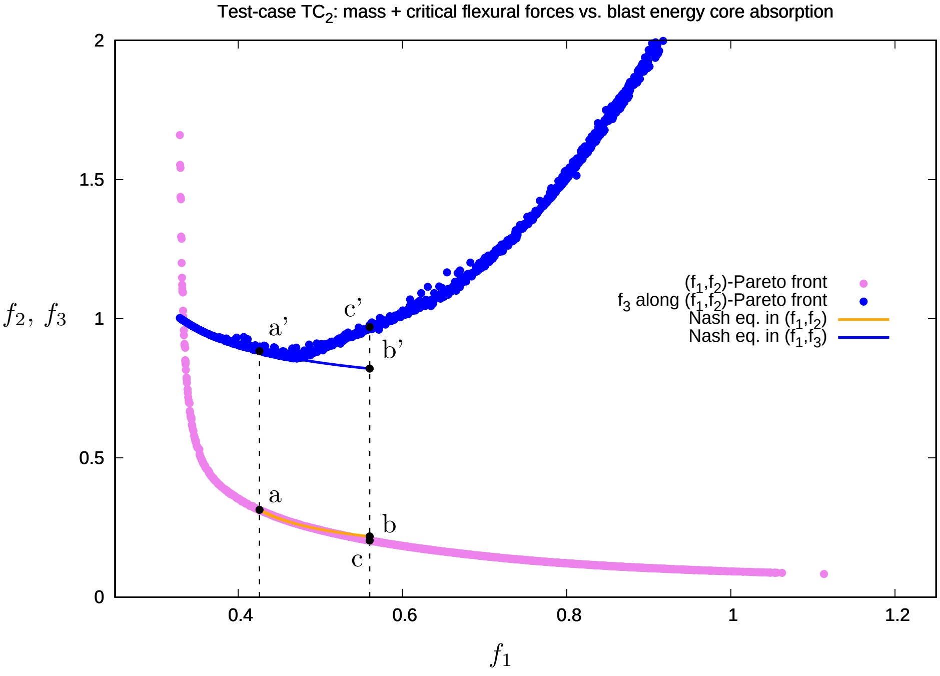

Figure 10: Test-case TC$_2$: Pareto front and continuum of Nash equilibria ($f_1 = \varphi_m$, $f_2 = \frac{1}{2}(\varphi_1 + \varphi_2)$, $f_3 = \frac{1}{2}e^{\varphi_u}$)

Here the secondary cost function was defined as $f_3 = \frac{1}{2}e^{\varphi_u}$. Recall that φ_u is inversely proportional to the blast energy absorption by the core. The function f_3 varies in the same direction; the exponential transform was found more stable; the factor $\frac{1}{2}$ has no effect on the convergence of the algorithm which in effect operates on logarithmic variables and is only used to scale the plot. (See Appendix B for more precisions on the merits of the exponential trannsform.)

The function f_3 was evaluated for the Pareto-optimal design-points as shown on Figure 10 in blue symbols. As mass increases, the trend of f_3 is found monotone-decreasing for the lighter designs ($f_1 < 0.47$, approximately), and monotone-increasing for the heavier ones ($f_1 > 0.47$).

As an example, the computation of a continuum of Nash equilibria devised to reduce f_3 was initiated from a design point for which $(f_1, f_2) \approx (0.4260, 0.3137)$ (point a on Figure 10), and $f_3 \approx 0.8832$ (point a'). The continuum is represented by a yellow curve in terms of (f_1, f_2) and a blue curve in terms of (f_1, f_3). The path in (f_1, f_2) remains close to the Pareto front, on the side of heavier designs, somewhat surprisingly (see final remarks). For example, at point b, mass has increased of some 31.5% (see Table 3). The cost function blending the flexural forces was reduced in about the same proportion (-30.5%). The secondary cost function, f_3 is notably reduced (-7.1%), which corresponds to an increase in the energy absorbed by the core (U_{lost}) of nearly 15%.

Test-case TC_2

ε	f_1	f_2	f_3	φ_u^{-1}
0.	0.4260	0.3137	0.8832	1.7576
0.9133	0.5602	0.2180	0.8208	2.0175
	(+31.5%)	(-30.5%)	(-7.1%)	(+14.8%)

Table 3: Values of the objective functions at start and near the end of the continuum ($\varphi_u^{-1} = 1/\ln(2f_3) \propto U_{\text{lost}}$)

Consider also the point c on the Pareto front corresponding to approximately the same mass as b. Although, b and c are close in (f_1, f_2), the value of f_3 at c' is about 0.97, that is 18% superior to the value at point b'.

Greater improvements could be achieved further down the continuum, at the cost of higher values of mass. This was not exploited more, since studying the criterion on deflection was considered of greater interest.

Other remarks

- Analysis of Figure 12

  The primary steering function curve, in black solid line, is tangent at the starting point to the ε axis, indicating that the Pareto stationarity is maintained to ε^2. The steering function dominates the two primary objective functions (in red and orange).

  The secondary objective function, in blue, has been evaluated a posteriori from the computed value of the vector $\overline{\mathbf{x}}_\varepsilon$ at the local Nash equilibrium point, by its exact model. It follows very closely the secondary steering function constructed from a global quadratic meta-model, demonstrating the accuracy of the meta-model. The dashed line is the initial tangent to the steering function. The initial logarithmic derivative of the secondary cost function, visualized by the slope of the tangent to the blue curve, is accurately predicted by the theory.

  The parameter $\varepsilon_{\max} = \min(\varepsilon_c, 1)$ where ε_c is the theoretical limit of convexity as computed by the software; it is here equal to 1.

  Overall, the figure illustrates the usual "funnel-shaped pattern" of the objective function plot.

- Analysis of Figure 13

  The figure depicts the variation with ε of the optimization variables along the continuum. The equilibrium is found mostly by increasing the thickness of the core (in blue). The upper surface thickness (in red) is maintained at lower bound (to augment the energy transfer to the core), while the lower surface thickness (in yellow) is somewhat diminished, and the ratio **R** (in green) increased. The slack variable (in violet) adjusts to these variations to satisfy the constraint on total thickness. This is not a desirable practical design, but it makes sense from an algorithmic viewpoint since the optimization has been conducted to maximise U_{lost}.

- Analysis of Figure 14

  The figure depicts the variation with ε of the constraint function $c_1(\mathbf{x})$ in (3). The plot indicates that the constraint is very accurately enforced over a large portion of the continuum ($|c_1| < 10^{-6}$), before instability is finally triggered.

Conclusion

This test-case has served again to demonstrate the potential of the prioritized optimization approach to reduce a secondary cost function while almost maintaining Pareto-optimality on the primary cost functions. However the designs achieved in this experiment are not practical since only the core blast energy absorption was considered in the optimization.

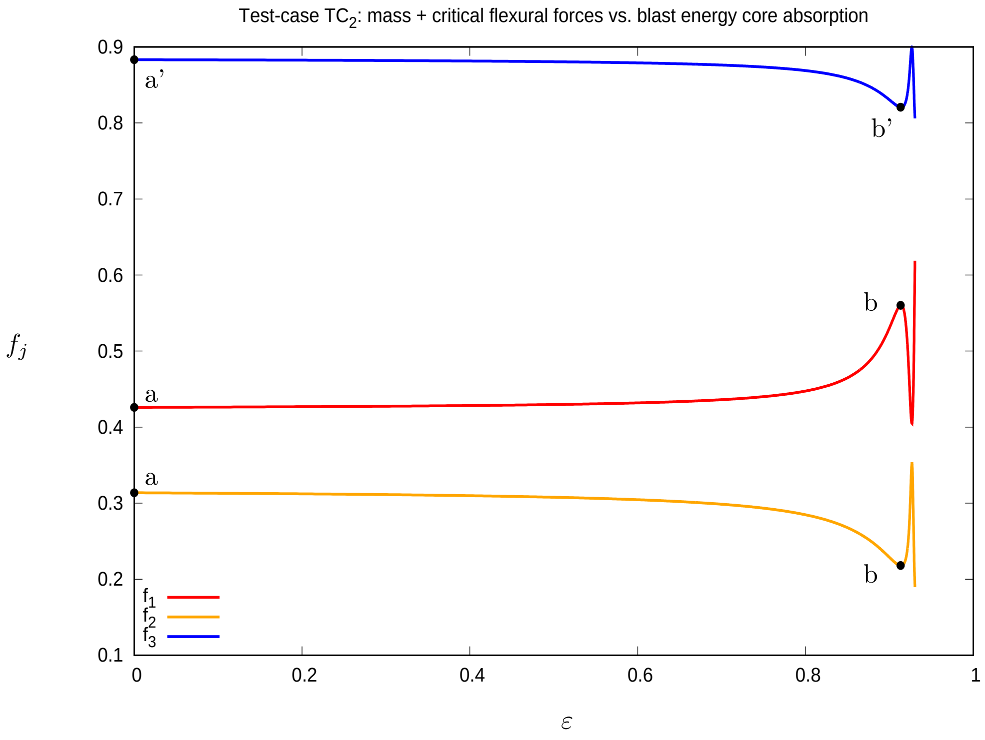

Figure 11: Test-case TC$_2$: Objective functions $\{f_j\}$ along the continuum in terms of the continuation parameter ε $(f_1 = \varphi_m,\ f_2 = \frac{1}{2}(\varphi_1 + \varphi_2),\ f_3 = \frac{1}{2}e^{\varphi_u})$

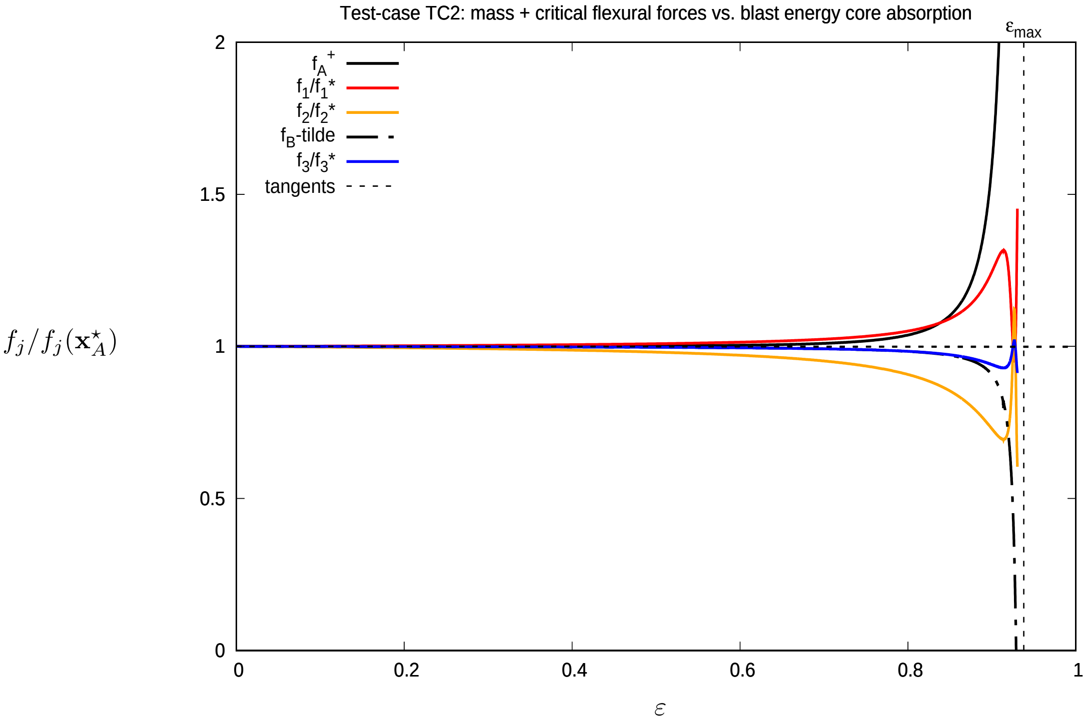

Figure 12: Test-case TC$_2$: Objective functions $\{f_j/f_j(\mathbf{x}_A^\star)\}$ along the continuum in terms of the continuation parameter ε $(f_1 = \varphi_m,\ f_2 = \frac{1}{2}(\varphi_1 + \varphi_2),\ f_3 = \frac{1}{2}e^{\varphi_u})$

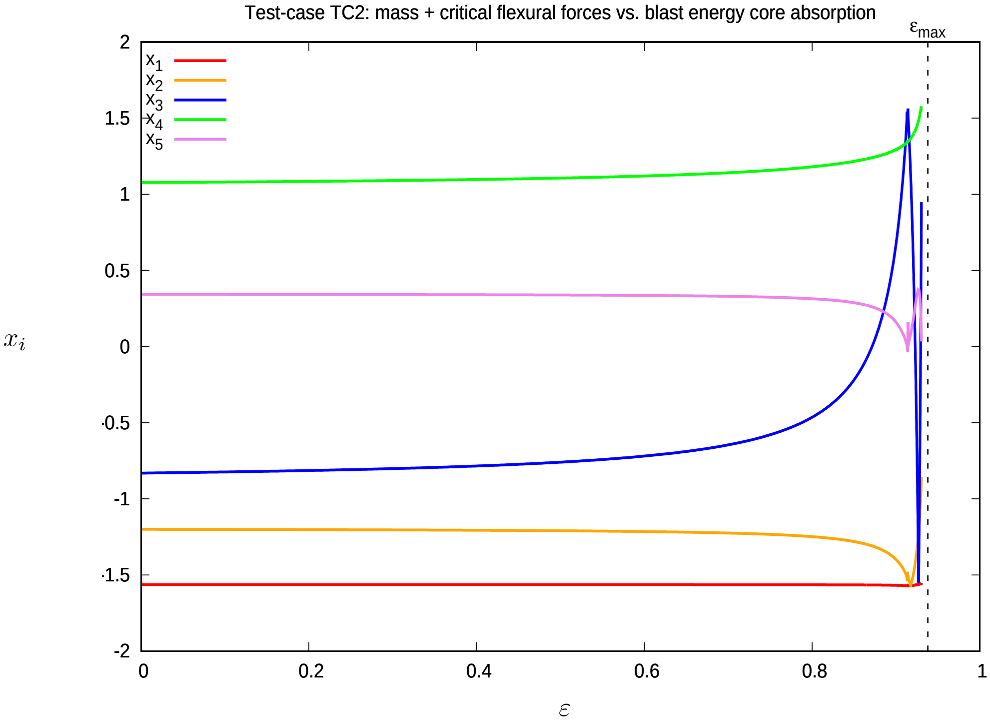

Figure 13: Test-case TC$_2$: Optimization variables $\{x_i\}$ along the continuum in terms of the continuation parameter ε $(f_1 = \varphi_m,\ f_2 = \frac{1}{2}(\varphi_1 + \varphi_2),\ f_3 = \frac{1}{2}e^{\varphi_u})$

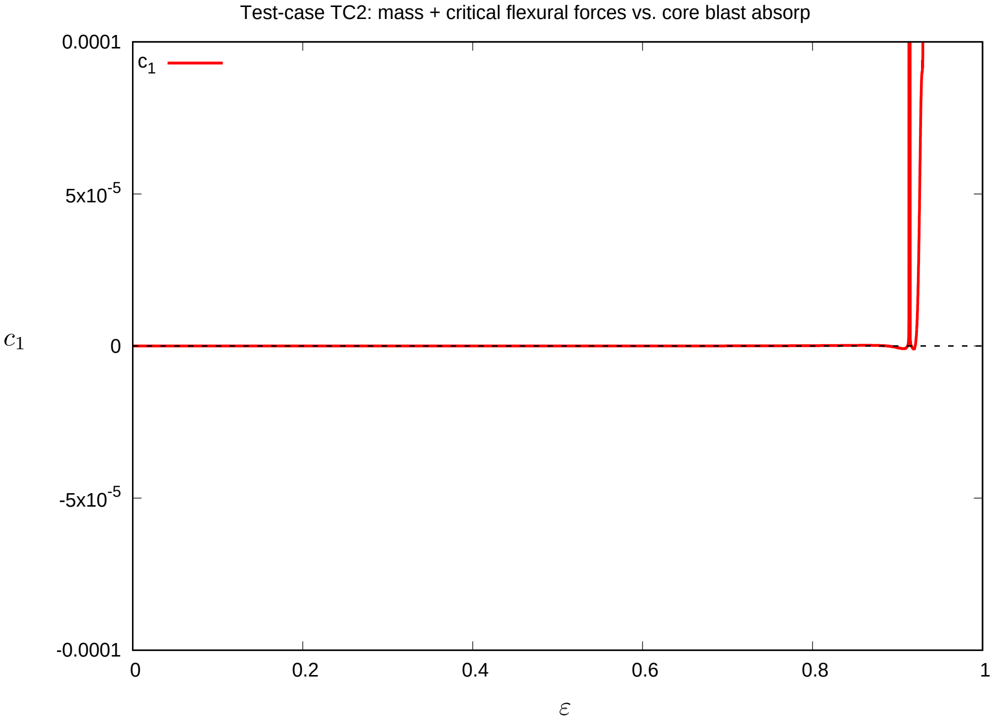

Figure 14: Test-case TC$_2$: Constraint function c_1 along the continuum in terms of the continuation parameter ε $(f_1 = \varphi_m,\ f_2 = \frac{1}{2}(\varphi_1 + \varphi_2),\ f_3 = \frac{1}{2}e^{\varphi_u})$

8 Test-case 3: Blast mitigation by reducing the deflection at the central point

The objective functions involved in this test-case have been defined in the third row of Table 1. As in TC$_2$, the primary cost functions are $f_1 = \varphi_m$ (mass) and $f_2 = \frac{1}{2}(\varphi_1 + \varphi_2)$ (blend of critical flexural forces). Now, the secondary cost function is $f_3 = \varphi_w$, proportional to the deflection at the element center due to blast.

The Pareto-front in (f_1, f_2) (same as in TC$_2$) and the values of the secondary cost function f_3 along it are shown on Figure 15. It appears that as mass increases, f_3 decreases rapidly for the lighter designs, and increases somewhat more moderately for the heavier ones.

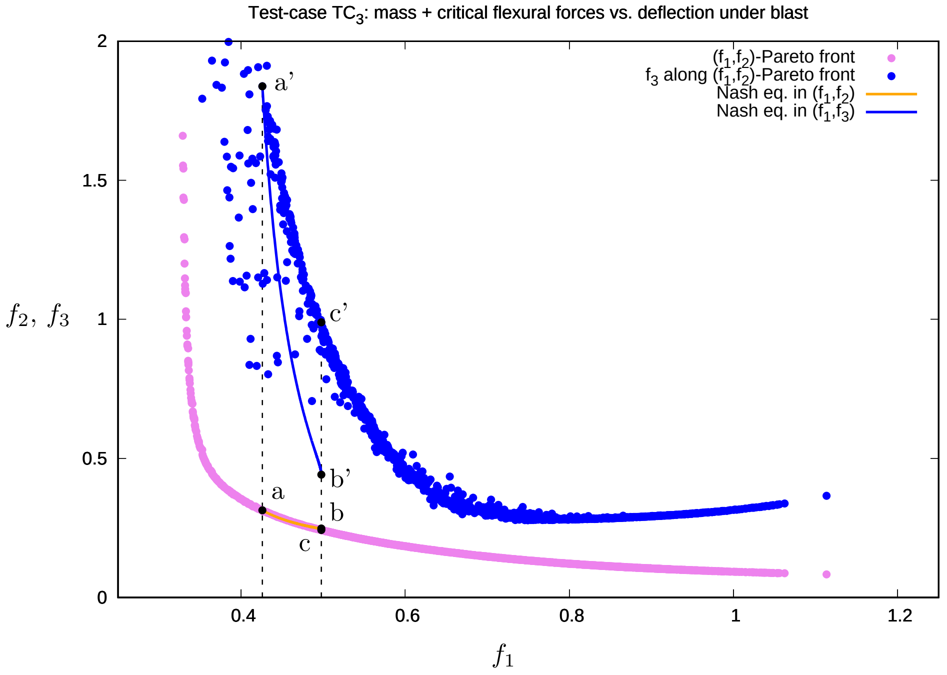

Figure 15: Test-case TC$_3$: Pareto front and continuum of Nash equilibria ($f_1 = \varphi_m$, $f_2 = \frac{1}{2}(\varphi_1 + \varphi_2)$, $f_3 = \varphi_w$)

The continuum of Nash equilibria was initiated again at point a of the Pareto front at which $(f1, f2) \approx (0.4260, 0.3137)$, and here $f_3 \approx 1.8378$ (point a') (see Table 4). At point b of the continuum of Nash equilibria, mass has increased of nearly 17%, the cost function based on critical flexural forces has been reduced of 21%, but even more impressively, the deflection w has been reduced by a factor of 4 (76%).

Test-case TC_3

ε	f_1	f_2	f_3
0.	0.4260	0.3137	1.8378
0.6500	0.4978 (+16.8%)	0.2478 (-21.0%)	0.4415 (-76.0%)

Table 4: Values of the objective functions at start and near the end of the continuum

Other remarks

- Further analysis of Figure 15

The values of the secondary cost function f_3 realized by the design-points constitutive of the Pareto front exhibit a notable sparsity: several data points appear closely to a given vertical line for fixed f_1, or closely to a given horizontal line for fixed f_2. Let us first explain this point. The Pareto front is here continuous and convex, and a generic point over it can be associated with a unique value $\alpha \in [0,1]$ for which the optimality of $(1-\alpha)f_1 + \alpha f_2$ under the contraint $c_1(\mathbf{x}) = 0$ writes:

$$\begin{cases} (1-\alpha)\nabla f_1(\mathbf{x}_\alpha) + \alpha \nabla f_2(\mathbf{x}_\alpha) + \lambda_1 \nabla c_1(\mathbf{x}_\alpha) = 0 \\ c_1(\mathbf{x}_\alpha) = 0 \end{cases} \tag{32}$$

in which λ_1 is a Lagrange multiplier, and it is assumed that $\nabla c_1(\mathbf{x}_\alpha) \neq 0$. Here $\mathbf{x}_\alpha$ denotes any point for which this is true. The above system is made of $n+1$ equations, and it involves $n+1$ unknowns: the n components of $\mathbf{x}_\alpha$ and λ_1. Hence the system is closed, but nonlinear. One can therefore expect that the system admits a finite number of solutions, for a given α.

Remark 1
One could also solve the following system for $\mathbf{x}_\alpha$

$$\begin{cases} f_1(\mathbf{x}_\alpha) = \overline{f_1} \\ f_2(\mathbf{x}_\alpha) = \overline{f_2} \\ c_1(\mathbf{x}_\alpha) = 0 \end{cases} \tag{33}$$

for a given point $(\overline{f_1}, \overline{f_2})$ *on the Pareto front corresponding to* α*. Presently, the system involves 5 unknowns and only 3 equations. Additionally, these equations are nonlinear. One can expect multiple solutions.*

Furthermore, the numerical determination of $\mathbf{x}_\alpha$ may also introduce noise, adding difficulty to identify $\mathbf{x}_\alpha$. Figure 16 shows the values of the optimization variables $\{x_i\}$ $(i = 1, \dots, 5)$ for the 1170 computed approximate Pareto-optimal solutions and it provides some numerical evidence of the Pareto set structure.

Hence, along the continuum, the objective function f_3 should be viewed as a multi-valued function of α (or f_1, or f_2). To support this, let us compare the values of the objective functions achieved at a point ã found very close to point a on the (numerical) Pareto front. The two points are defined in Table 5 and cannot be distinguished visually on Figure 15. However, these points are the images of very different vectors $\mathbf{x}_a$ and $\mathbf{x}_{\tilde{a}}$ given in Table 6 and, unsurprisingly, they produce very different values of f_3:

$$f_3(\mathbf{x}_\mathrm{a}) = 1.8378029080250435356, \quad f_3(\mathbf{x}_{\tilde{\mathrm{a}}}) = 1.1279592785444769 7314. \tag{34}$$

In Appendix C, the prioritized optimization technique is applied to initiate a continuum from point $\mathbf{x}_a$, targeting the (f_1, f_2) function values of $\tilde{a}$, and remaining very close to the

	Point a	Point ã
f_1	0.42598809609657090	0.42635839249323715
f_2	0.31366257168969769	0.31029049664324115
f_3	1.8378029080250435	1.1279592785444770

Table 5: Points a and ã on the Pareto front and corresponding values of f_3

$\mathbf{x}_a$	$\mathbf{x}_{\tilde{\mathrm{a}}}$
-1.5629544943845421	-1.4144970591997961
-1.2000870006928384	-1.3793914064570238
-0.83094529619039448	-0.42727195797380824
1.0769290088008954	0.64200154487802674
0.34345599756029616	0.31198142859396794

Table 6: Vectors associated with the Pareto-optimal points a and ã

Pareto front. The exercise permits to calculate a point $\overline{\mathbf{x}}$ in the domain, whose image $\bar{a}$ is even closer to $\tilde{a}$ than a, although $\overline{\mathbf{x}}$ is closer in structure and figures to $\mathbf{x}_a$, and corresponds to an f_3 value close to that of $\mathbf{x}_a$, and not $\mathbf{x}_{\tilde{a}}$.

Examining again Figure 15, it appears that point b' is not as efficient in blast mitigation as a point c' obtained by "sliding along the Pareto front" from point a' downwards. However such slide is not such a misleading concept.

Firstly, the above conclusion could have been inverse if the comparison had been made at an earlier stage of the continuum, to the left of the intersection point between the blue line and the blue symbols.

Secondly, and more dramatically, if the Pareto front had been computed less densely and less accurately, as it is usually the case when the computational cost of evaluation of the functions is large, due to the sparsity of the data points, and the multi-valued character of computed $f_3(\alpha)$ (or $f_3(f_1)$), the appropriate strategy might not have appeared straightforwardly.

This demonstrates that even when a portion of the Pareto front of the primary objective functions is known approximately, that is, not very densely or accurately identified, the strategy for deciding for an appropriate small slide over it on the basis of the evaluation of a secondary objective function, may not be so clear.

After electing a central point on the Pareto front, one may look for a point to its left, and for one to its right, and compare associated values of f_3. But these may not correspond to roots, that is, solutions of (32), that can be matched by continuity. If so, the comparison is only valid for these particular points, and may induce questionable information about trends.

Alternately, computing and analyzing, e.g. by self-organizing maps, a Pareto front for the whole set of objective functions, primary and secondary ones altogether, could result in an excessive endeavor.

Note that in the present approach, the local behavior of f_3 is accounted for via a local metamodel of 5 variables, not restricted to the Pareto set. The continuum of Nash equilibria seems to be able to find the advantageous direction, at small computational effort, and respecting the natural hierarchy among the objective functions.

- Analysis of Figures 17-18

  The figures indicate the variation in absolute and relative values of the three objective functions along the continuum. Note on Figure 18 how accurately f_3 follows the metamodel-based secondary steering function f_B in values, tangent and convexity.

- Analysis of Figure19

  The figure indicates that in the Nash game the three thicknesses have noticeably different variations. Again the core size (in blue) is enhanced, but here the upper surface is slightly made thicker. The lower surface is again made thinner; the ratio **R** is reduced, and x_5 adjusts to the constraint.

- Analysis of Figure20

  Along the continuum and before instability is triggered, the constraint is accurately satisfied: $|c_1| < 10^{-5}$.

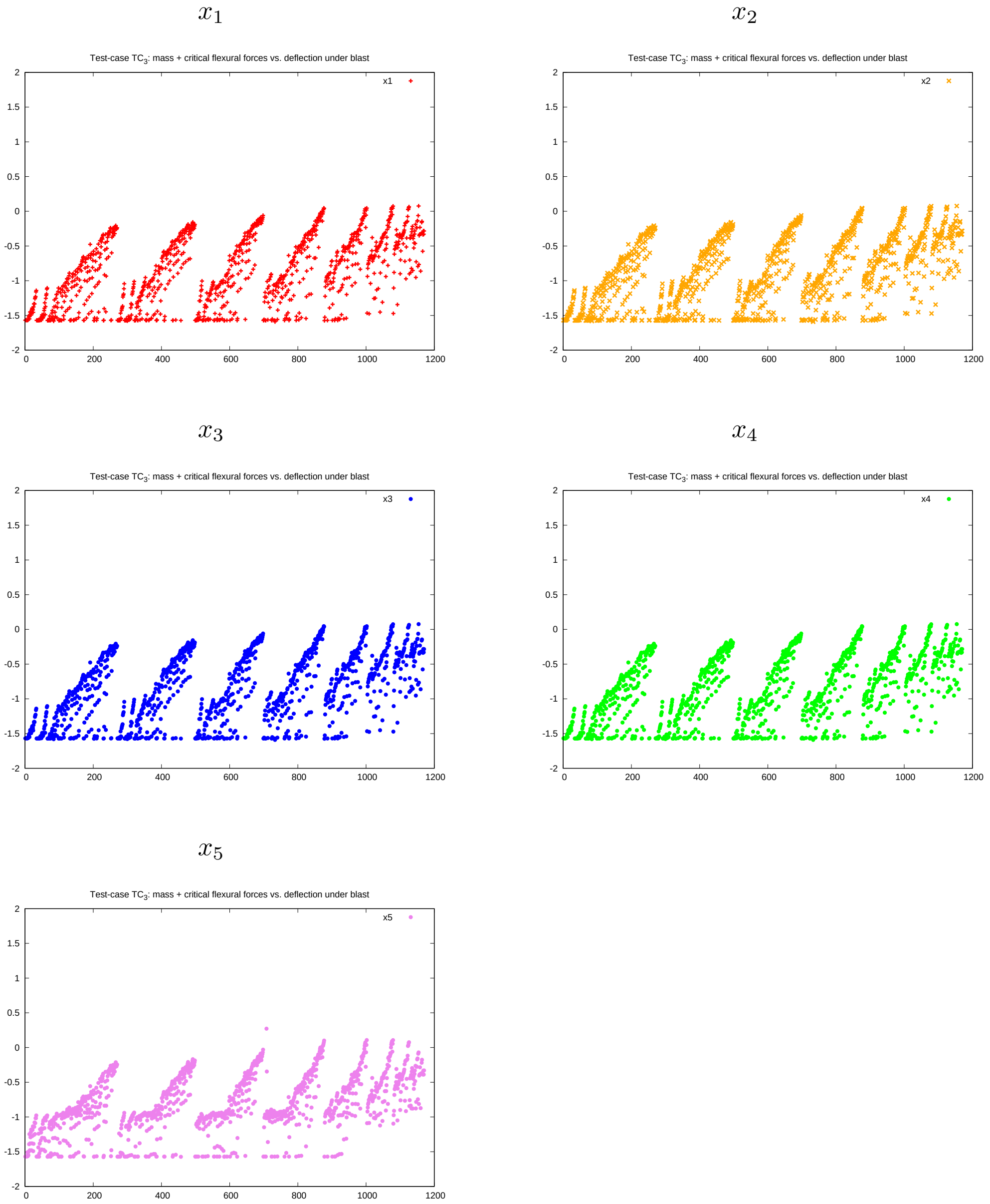

x_1 x_2 x_3 x_4 x_5

Figure 16: Test-case TC$_3$: Pareto set

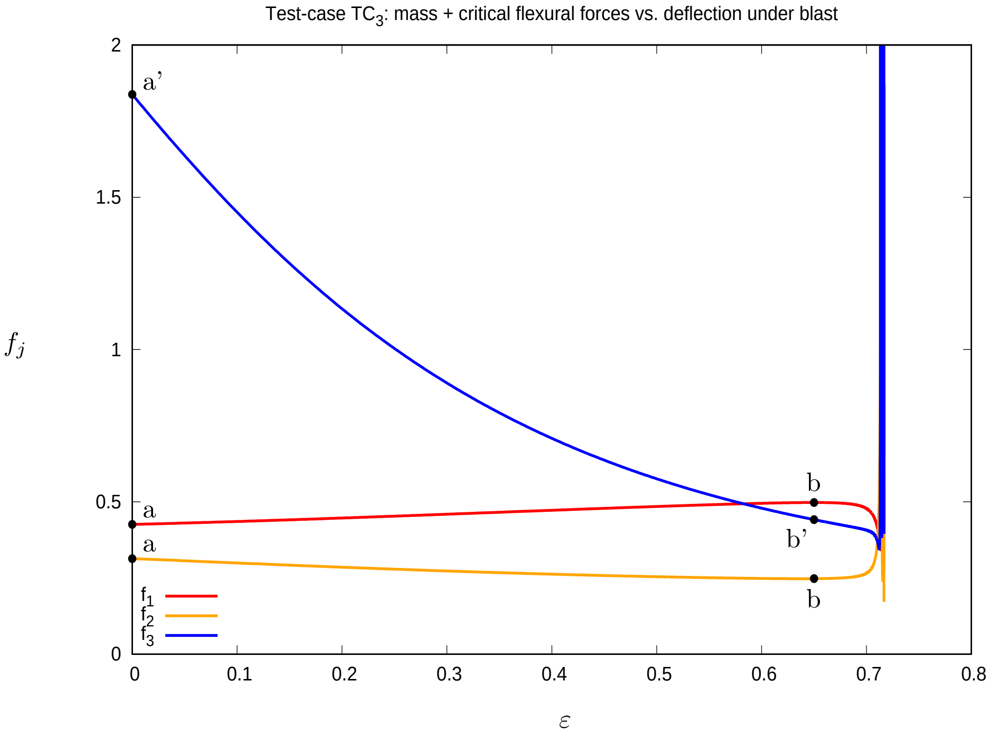

Figure 17: Test-case TC$_3$: Objective functions $\{f_j\}$ along the continuum in terms of the continuation parameter ε $(f_1 = \varphi_m,\ f_2 = \frac{1}{2}(\varphi_1 + \varphi_2),\ f_3 = \varphi_w)$

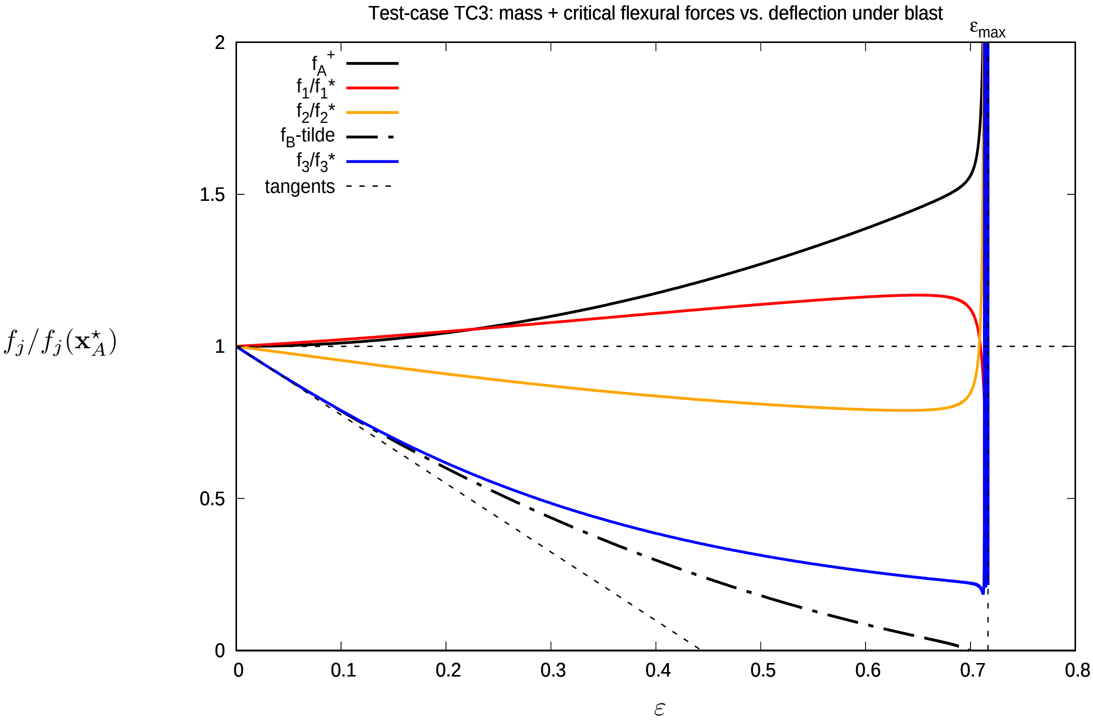

Figure 18: Test-case TC$_3$: Objective functions $\{f_j/f_j(\mathbf{x}_A^\star)\}$ along the continuum in terms of the continuation parameter ε $(f_1 = \varphi_m,\ f_2 = \frac{1}{2}(\varphi_1 + \varphi_2),\ f_3 = \varphi_w)$

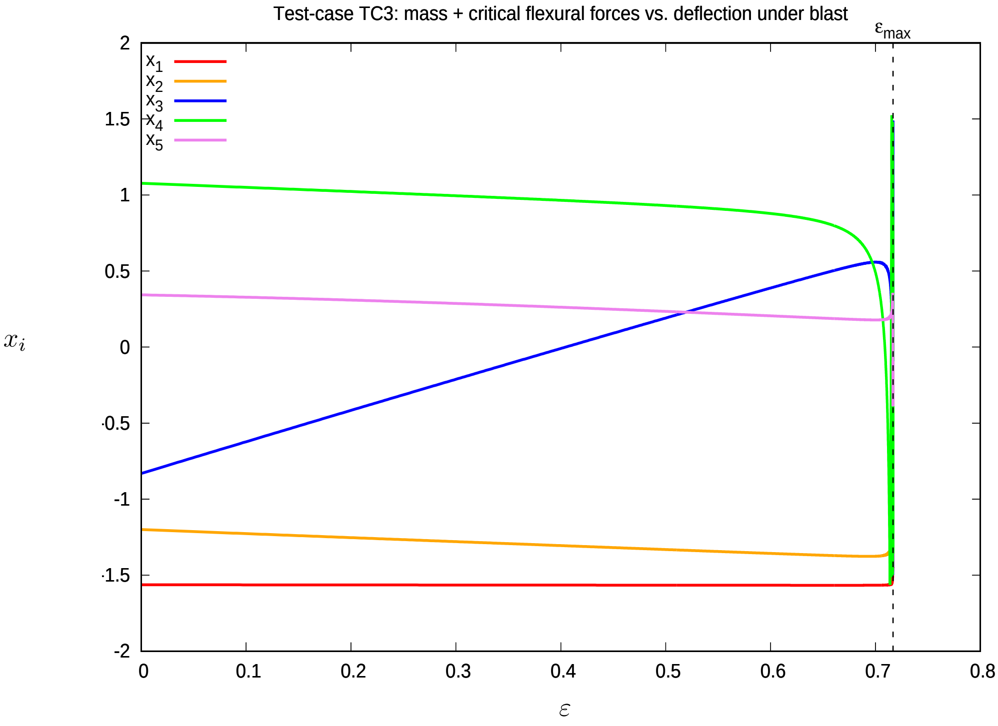

Figure 19: Test-case TC_3: Optimization variables $\{x_i\}$ along the continuum in terms of the continuation parameter ε $(f_1 = \varphi_m,\ f_2 = \frac{1}{2}(\varphi_1 + \varphi_2),\ f_3 = \varphi_w)$

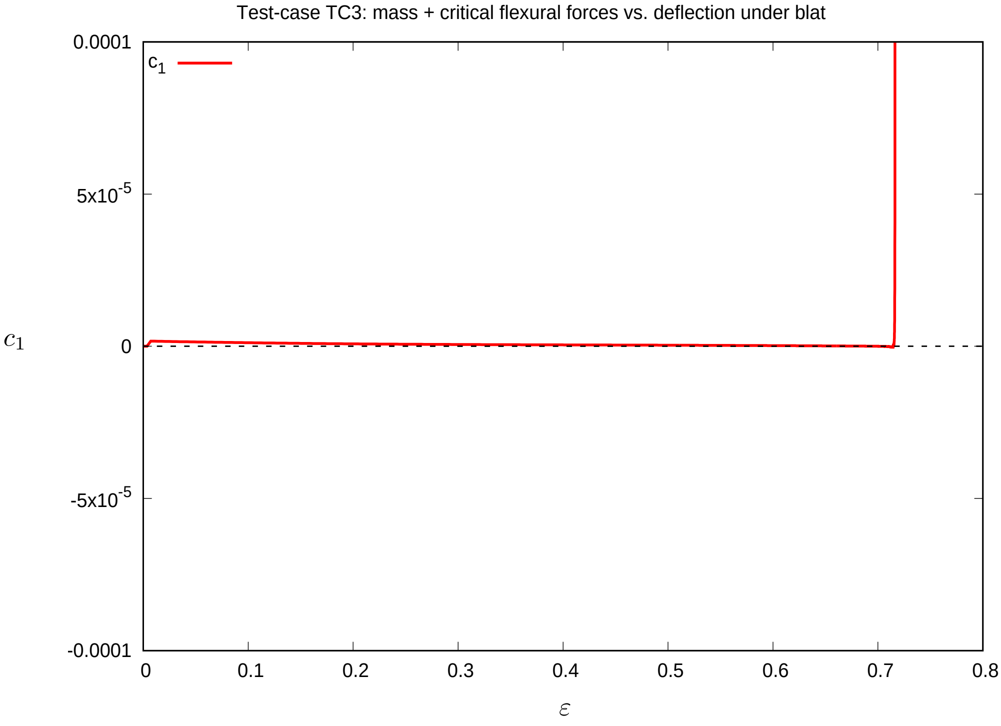

Figure 20: Test-case TC_3: Constraint function c_1 along the continuum in terms of the continuation parameter ε $(f_1 = \varphi_m,\ f_2 = \frac{1}{2}(\varphi_1 + \varphi_2),\ f_3 = \varphi_w)$

Conclusion

The optimization conducted in the treatment of Test-case TC_3, has involved a more relevant global secondary cost function, successfully accounted for by the prioritized optimization approach.

9 Test-case 4: Blast mitigation by simultaneously augmenting the core energy absorption and reducing the deflection at the central point

This test-case is a variation of Test-case TC_3 intended to account for both physical measures of blast mitigation in relation to w and U_{lost}. The objective functions have been defined in the fourth row of Table 1. As in TC_2 and TC_3, the primary cost functions are $f_1 = \varphi_m$ (mass) and $f_2 = \frac{1}{2}(\varphi_1 + \varphi_2)$ (blend of critical flexural forces). Now, the secondary cost functions are two: $f_3 = \varphi_w$ that is proportional to the deflection at the element center due to blast, and $f_4 = \frac{1}{2}e^{\varphi_u}$ that is inversely proportional the core blast energy absorption.

The Pareto-front in (f_1, f_2) is the same as in TC_2 and TC_3. It is shown on Figure 21, as well as the values of the secondary cost functions (f_3, f_4) (for the Pareto-optimal design-points). It appears that as mass increases, the general trend of both secondary cost functions indicates first a decay to a minimum and then an increase, as it was previously observed since the Pareto optimal design-points are the same.

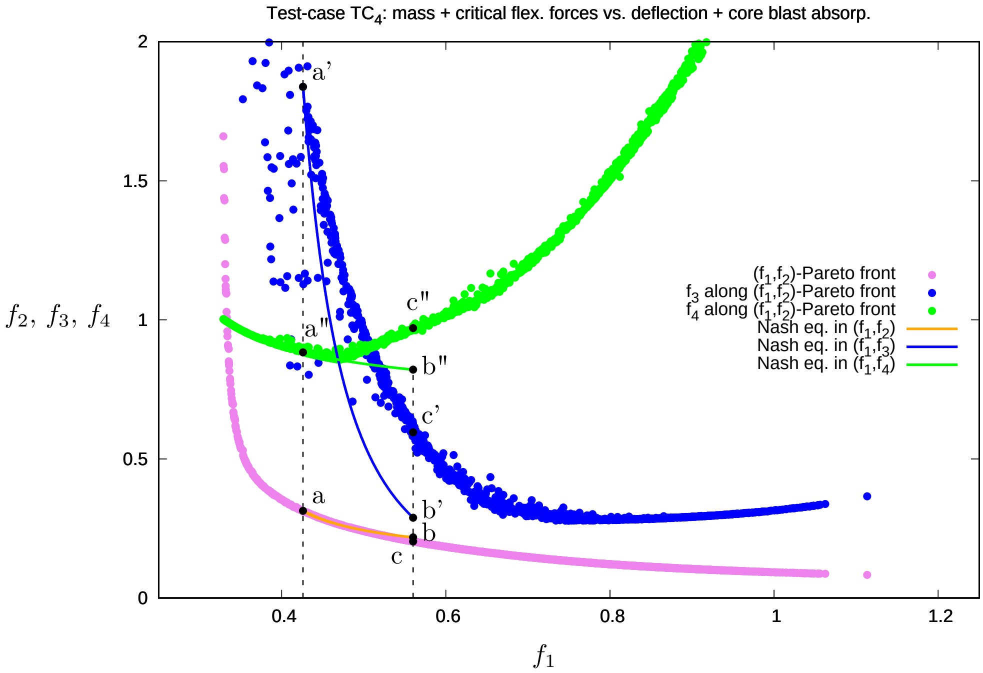

Figure 21: Test-case TC_4: Pareto front and continuum of Nash equilibria ($f_1 = \varphi_m$, $f_2 = \frac{1}{2}(\varphi_1 + \varphi_2)$, $f_3 = \varphi_w$, $f_4 = \frac{1}{2}e^{\varphi_u}$)

For example, at point b, mass has increased of some 32%, the cost function based on critical flexural forces diminished of about 31%, the deflection w of more than 84%, and f_4, based on the core blast energy absorption, significantly (7%) corresponding to nearly 15% increase in flexural forces (see Table 7).

Test-case TC_4

ε	f_1	f_2	f_3	f_4	φ_u^{-1}
0.	0.4260	0.3137	1.8380	0.8832	1.7576
0.9133	0.5602	0.2180	0.2885	0.8208	2.0175
	(+31.5%)	(-30.5%)	(-84.3%)	(-7.1%)	(+14.8%)

Table 7: Test-case TC_4: Values of the objective functions at start and near the end of the continuum ($\varphi_u^{-1} = 1/\ln(2f_4) \propto U_{\mathrm{lost}}$)

Other remarks

- Analysis of Figure 23

  The figure confirms that the functions $f_3(\varepsilon)/f_3^\star$ and $f_4(\varepsilon)/f_4^\star$ are osculatory to the secondary steering function $f_B(\varepsilon)$ at the starting point of the continuum ($\varepsilon = 0$). However, their common derivative is initially very small. This is because, in the MGDA construction of $f_B = \alpha_3 f_3/f_3^\star + \alpha_4 f_4/f_4^\star$, the vector of coefficients $\alpha = (\alpha_3, \alpha_4)$ is determined by seeking for the minimum-norm element in the convex hull of the logarithmic gradients $(\nabla f_3/f_3^\star, \nabla f_4/f_4^\star)$, that is: $\min_\alpha \|\nabla f_B\|$ subject to $\alpha_3 + \alpha_4 = 1$. When the norms of the gradients are very different, it is the gradient of smaller magnitude, here $\nabla f_4/f_4^\star$, that mostly influences the resulting α, and determines the common initial derivative. However, the global reduction of f_3 is actually far greater than this initial derivative would suggest. Also note that the concavity of $f_3(\varepsilon)$ has changed in comparison with TC_3.

- Analysis of Figure 24

  The figure shows that the Nash game affects all five variables. In comparison with TC_3, the core thickness also increases but differently, and the ratio $\mathbf{R}$ here augments somewhat.

- Analysis of Figure 25

  Apart from the very end of the continuum, when the instability is triggered, the constraint violation function $|c_1(\mathbf{x})|$ remains less than 10^{-6}, two orders of magnitude inferior to the accuracy tolerance.

Conclusion

The prioritized optimization process was able to diminish both blast-mitigation-related objective functions. The reduction in deflection is impressive, the increase in energy absorption by the core more moderate, but significant.

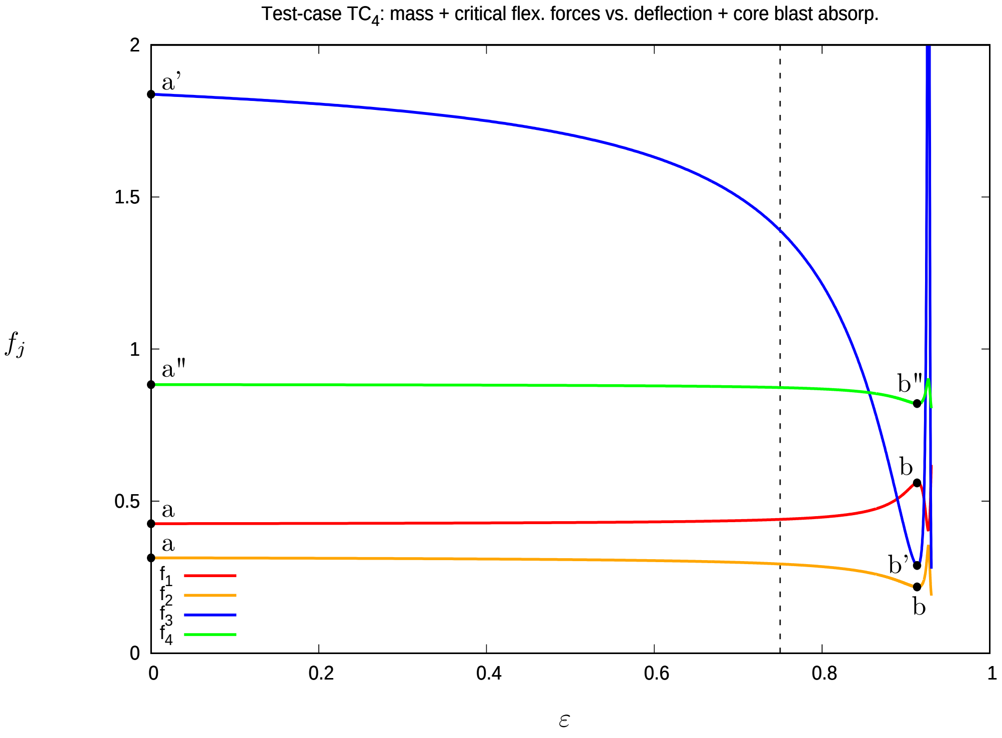

Figure 22: Test-case TC_4: Objective functions $\{f_j\}$ along the continuum in terms of the continuation parameter ε $(f_1 = \varphi_m,\ f_2 = \frac{1}{2}(\varphi_1 + \varphi_2),\ f_3 = \varphi_w,\ f_4 = \frac{1}{2}e^{\varphi_u})$

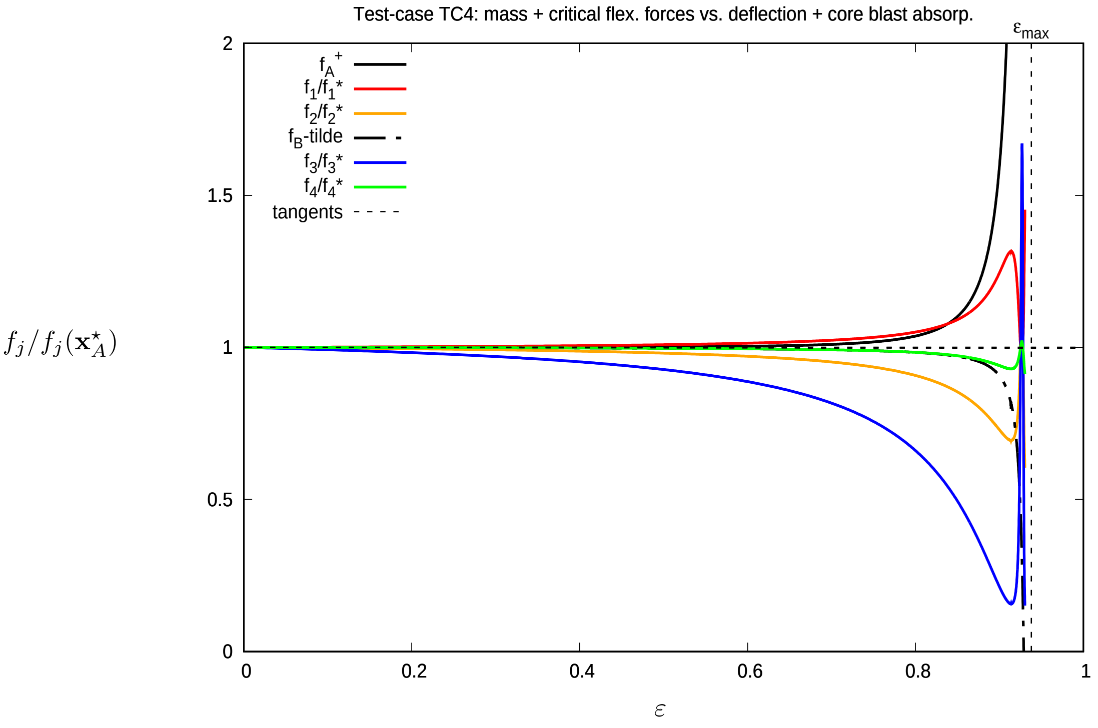

Figure 23: Test-case TC_4: Objective functions $\{f_j/f_j(\mathbf{x}_A^\star)\}$ along the continuum in terms of the continuation parameter ε $(f_1 = \varphi_m,\ f_2 = \frac{1}{2}(\varphi_1 + \varphi_2),\ f_3 = \varphi_w,\ f_4 = \frac{1}{2}e^{\varphi_u})$

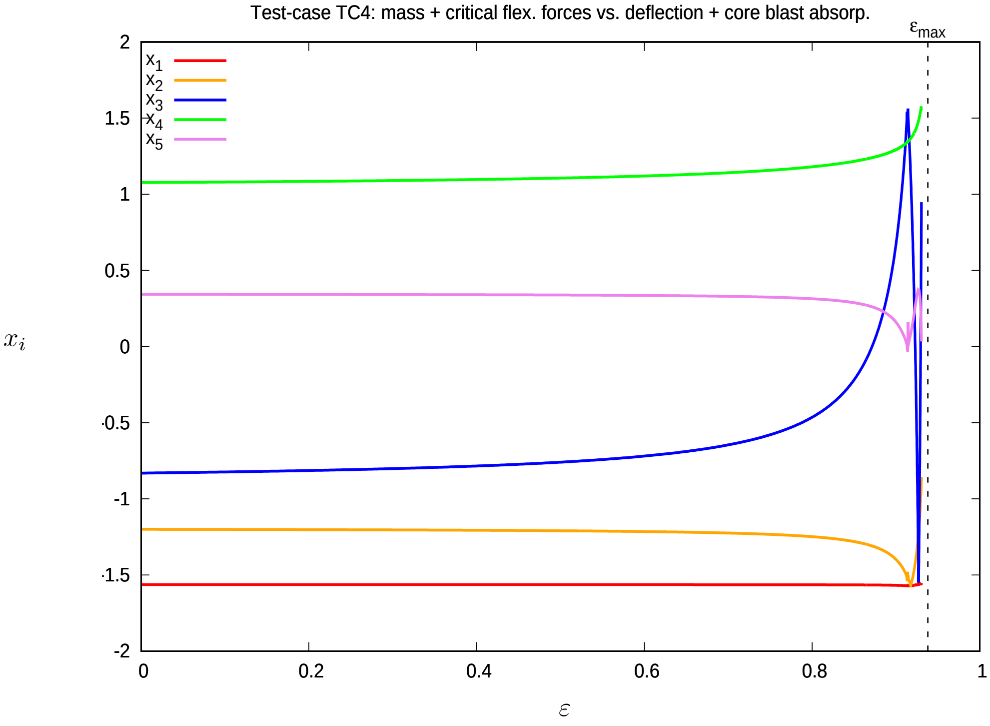

Figure 24: Test-case TC$_4$: Optimization variables $\{x_i\}$ along the continuum in terms of the continuation parameter ε $(f_1 = \varphi_m,\ f_2 = \frac{1}{2}(\varphi_1 + \varphi_2),\ f_3 = \varphi_w,\ f_4 = \frac{1}{2}e^{\varphi_u})$

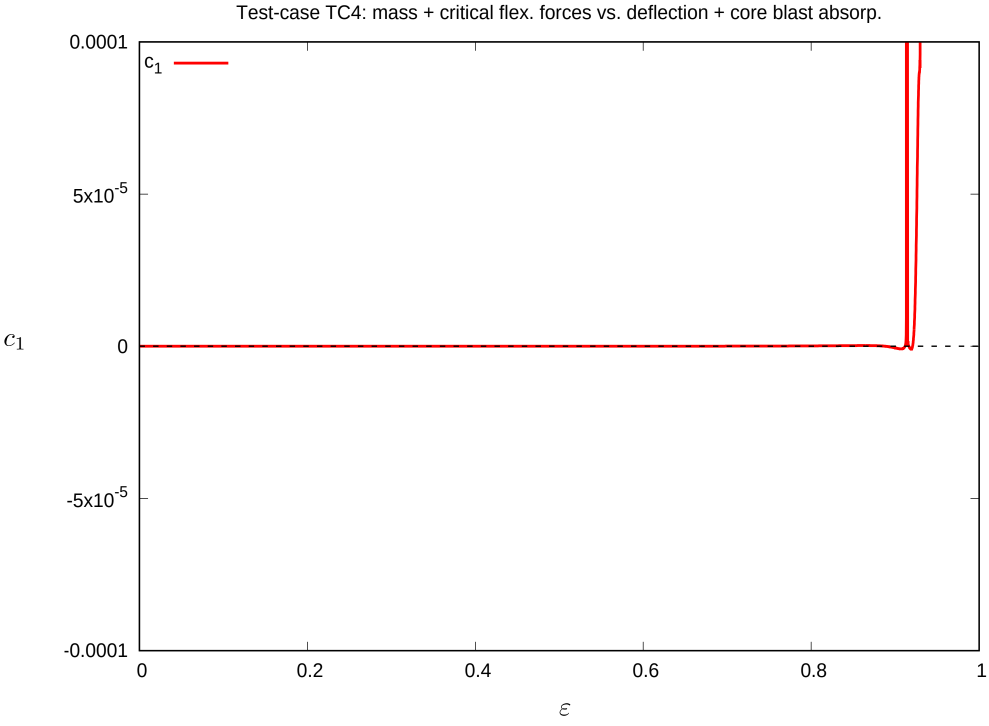

Figure 25: Test-case TC$_4$: Constraint function c_1 along the continuum in terms of the continuation parameter ε $(f_1 = \varphi_m,\ f_2 = \frac{1}{2}(\varphi_1 + \varphi_2),\ f_3 = \varphi_w,\ f_4 = \frac{1}{2}e^{\varphi_u})$

10 Conclusion

A sandwich panel structural model has been used to demonstrate the potential of a prioritized multi-objective optimization approach conducted to

- minimize mass,
- maximize critical flexural forces (first two modes),
- maximize the core energy absorption under blast,
- minimize the deflection at the element center under blast.

It was shown that the numerical method could be used to equate the two critical flexural forces, while almost maintaining Pareto optimality with mass. This constitutes an alternative to the non-differentiable optimization process consisting of maximizing the minimum.

From a point of Pareto optimality between mass and a blended measure of the critical flexural forces, a continuum of designs could be identified that improve the robustness of the element to blast with respect to either criterion, or both together. It is believed that the present approach is simpler than computing and analyzing the enhanced Pareto front associated with the four objective functions together, particularly in the perspective of computationally demanding applications.

An interesting point was observed in the treatment of Test-case TC3. Once the (f_1, f_2) Pareto front is established, the evaluation of a secondary cost function, say f_3, at the Pareto-optimal design-points, may yield a very diverse and sparse set of values. This is because of two phenomena. First, and more fundamentally, several design- points may result in the same point on the Pareto front in function space. Second, the numerical treatment usually brings additional inaccuracy and sparsity. Here, the Pareto front was defined numerically in dense and accurate manner; still, the set of f_3 values was observed to be sparse. Hence, in more general cases, these numerical values may be very difficult to sort out, and the election of a design-point on the Pareto front on this sole basis, very hazardous.

In our experiment, the Nash game approach was relying more globally on the construction of a meta-model, accounting for the dependency on all of the variables and not restricted to Pareto optimal design-points . The calculated continuum of Nash equilibria was observed to be able to identify a favorable direction of search.

From a purely algorithmic viewpoint, as in [4], the general features of the prioritized optimization approach have been again verified. In particular, as the continuation parameter ε varies, the following observations can be made:

- The construction of the primary steering function is such that its derivative is equal to zero at the starting point, and this insures that the Pareto-optimality condition of the primary objective functions is only degraded by a term $O(\varepsilon^2)$.
- All secondary objective functions, following the constructed secondary steering function, evolve initially linearly with ε, with the same logarithmic derivative, $-\sigma$, where the positive constant σ is defined by theory and calculated numerically.

As a result, altogether the objective functions expressed as ratios to their respective initial values, exhibit a funnel-shaped pattern. Near the maximum value of ε for which convexity is established, an instability is usually triggered, in relation the local treatment of the constraint. However the interesting designs are found before, respecting accurately the constraint by the technique of the slack variable.

In the future, attempt will be made to apply the approach to a PDE-constrained optimization context in which the evaluation of the objective functions is necessarily more computationally demanding. In such a case, our plan is to develop additionally local surrogate models valid in the vicinity of the point chosen to initiate the continuum.

A Parameter setting used in the second phase of optimization

The starting point $\mathbf{x}_A^\star$ used to initiate the second phase of optimization conducted to reduce the secondary objective function f_3, as well as f_4 in Test-case TC_4, are defined in Table 8.

Test-case TC_1	Test-cases TC_2, TC_3 & TC_4
-1.57076160991465552108	-1.5629544943845421
-1.57079687643454857238	-1.2000870006928384
-1.49097112912103946236	-0.83094529619039448
0.41560914105402640972	1.0769290088008954
0.37386775227505097963	0.34345599756029616

Table 8: Components of the starting point $\mathbf{x}_A^\star$ of the continuum

The other numerical parameters have been set to the same values in all cases, except for mtot (total number of objective functions) equal to 4 in TC_4. These parameters are indicated in Table 9 which reproduces the file `my_testcase.dat` corresponding to Test-case TC_1.

```
testcase (character*80) :
Test-case TC_1; mass and critical flexural forces (1st and 2nd modes)

ndim
5

np
2

mfun
2

mtot
3

kc
1

xa_star
-1.57076160991465552108
-1.57079687643454857238
-1.49097112912103946236
0.41560914105402640972
0.37386775227505097963

hfdiff
1.d-2

hbox
1.d0

Bkappa
1.5d0

lstepmax
1000

eps1_over_epsmax
5.d-3

TOL
1.d-4

Lambdamax
10

mumax
5
```

Table 9: Parameter setting in Test-Case TC_1 in phase 2 of optimization

B On the exponential transform

Let $\phi(\mathbf{x})$ be a cost function to be minimized. It may be advantageous to replace this function by the following one for the purpose of a better-conditioned equivalent minimization:

$$\psi(\mathbf{x}) = e^{\lambda(\phi(\mathbf{x})-\phi_0)} \tag{35}$$

in which λ is an adjustable positive constant, $\mathbf{x}_0$ a reference point, and $\phi_0 = \phi(\mathbf{x}_0)$. Then:

- **Regularity:**
  The functions $\phi(\mathbf{x})$ and $\psi(\mathbf{x})$ have the same regularity since the exponential function is entire.
- **Values:**
  $$\psi(\mathbf{x}) > 0 \quad (\forall \mathbf{x}), \quad \psi(\mathbf{x}_0) = 1. \tag{36}$$
  The positivity of $\psi(\mathbf{x})$ may be a safeguard in case a logarithmic formulation is used, as it is the case in the present prioritized optimization approach. In such a case, $\psi(\mathbf{x})$ may also be multiplied by an arbitrary scaling factor without any consequence on the convergence.
- **Variation:**
  The functions $\phi(\mathbf{x})$ and $\psi(\mathbf{x})$ vary in the same way since the exponential function is uniformly monotone increasing.
- **Gradient:**
  $$\nabla\psi(\mathbf{x}) = \lambda e^{\lambda(\phi(\mathbf{x})-\phi_0)} \nabla\phi(\mathbf{x}) \tag{37}$$
  Hence
  $$\nabla\psi_0 = \lambda \nabla\phi_0 \tag{38}$$
  in which the subscript $_0$ indicates an evaluation at $\mathbf{x} = \mathbf{x}_0$.
- **Hessian:**
  $$\nabla^2\psi(\mathbf{x}) = \lambda e^{\lambda(\phi(\mathbf{x})-\phi_0)} \nabla^2\phi(\mathbf{x}) + \lambda^2 e^{\lambda(\phi(\mathbf{x})-\phi_0)} \nabla\phi(\mathbf{x}) \nabla\phi(\mathbf{x})^t \tag{39}$$
  in which the gradients are viewed as column-vectors, and the superscript ^{t} indicates transposition. Hence:
  $$\nabla^2\psi_0 = \lambda \left(\nabla^2\phi_0 + \lambda \nabla\phi_0 \nabla\phi_0^t \right). \tag{40}$$

The matrix $\nabla\phi_0 \nabla\phi_0^t$ is real-symmetric semi-definite-positive. If $\nabla\phi_0 \neq 0$, it is of rank 1. It only acts in the direction of $\nabla\phi_0$. In this direction, the quadratic form associated to it is positive. Thus the additional term tends to increase convexity, but in this direction only. Nevertheless, this effect may facilitate the numerical minimization of the cost function. In particular, if the minimization is conducted in the direction of vector $(-\omega)$, the constant λ should be chosen such that

$$\omega^t \left(\nabla^2\phi_0 \right) \omega + \lambda \left(\nabla\phi_0^t \, \omega \right)^2 > 0 \tag{41}$$

which is satisfied for sufficiently large λ, provided the direction of search $(-\omega)$ is not orthogonal to the gradient $\nabla\phi_0$ (or $\nabla\psi_0$). Evidently, this condition is not restrictive when minimizing $\phi(\mathbf{x})$ or $\psi(\mathbf{x})$.

C Closer examination of the (f_1, f_2) Pareto front

In Section 8, we observed that a given point on the (f_1, f_2)-Pareto front could be the image in function space of multiple elements of the Pareto set in the admissible domain. This appendix is intended to bring additional numerical evidence of this claim.

The question arises because after determining a Pareto front, or just a few points on it, one should look for a sensible additional criterion to elect one specific design point. This task may not be trivial when the points are scarce or inaccurate. This role may be devolved to f_3 in the priorized optimization approach. However, we claim that several values of f_3 can be associated with one given point on the Pareto front rendering the task possibly delicate.

Ideally, in order to demonstrate the multiplicity, one should solve the optimality conditions (32) for a given α and exhibit multiple solutions. However, we are not doing this exactly here. Firstly we replace the phrase "for a given α" by the equivalent phrase "for a given f_1" (mass). Secondly, to simplify the numerical experiment, we approximate locally the Pareto front by a small arc of a continuum of Nash equilibria, presumably tangent to it, originating from a chosen point.

The notations of Section 8 are used again, except for f_3 to which a different definition is given. The prioritized optimization technique is used here to calculate a point $\overline{\mathbf{x}}$, nearly Pareto-optimal in (f_1, f_2), close in structure and figures to $\mathbf{x}_{\mathrm{a}}$, but at the abscissa of ã, that is, such $f_1(\overline{\mathbf{x}}) = f_1(\mathbf{x}_{\tilde{\mathrm{a}}})$ (very accurately), although $\overline{\mathbf{x}}$ is quite different from $\mathbf{x}_{\tilde{\mathrm{a}}}$, and corresponding values of f_3 as well.

In this prioritized optimization experiment, the function f_3 is here defined as follows:

$$f_3(\mathbf{x}) = |f_1(\mathbf{x}) - f_1(\mathbf{x}_{\tilde{\mathrm{a}}})| \,. \tag{42}$$

The variation of the objective functions over a small initial portion of the continuum is visualized on Figure 26. The function f_3 achieves a minimum nearly equal to 0 ($< 10^{-6}$) at the following point

$$\begin{aligned} \overline{\mathbf{x}} = (&-1.5630812029242649, -1.2044701136340688, -0.82349207642836941, \\ &1.0993200580621512, 0.34306814181817574) \end{aligned} \tag{43}$$

at which the function values are:

$$\begin{cases} f_1(\overline{\mathbf{x}}) = 0.42635819753843 79 \\ f_2(\overline{\mathbf{x}}) = 0.31295990093856402 \\ \varphi_u(\overline{\mathbf{x}}) = 1.8292653027492944 \end{cases} \tag{44}$$

The distance (in function space) between $(f_1(\overline{\mathbf{x}}), f_2(\overline{\mathbf{x}}))$ and ã is 2.7×10^{-3}, that is, "small", while the distance (in the domain) between their respective origins, $\overline{\mathbf{x}}$ and $\mathbf{x}_{\tilde{\mathrm{a}}}$, is close to 0.65, that is, "finite", and the corresponding values of φ_u are evidently different (1.829 and 1.128). The approximate configuration of points points a, ã and $\overline{\mathbf{x}}$ is sketched in Figure 27.

The calculation of the continuum was performed using the rather unusual setting of parameters defined in Table 10

Lastly, note that the experiment has also illustrated the potential of the prioritized approach to handle certain target problems.

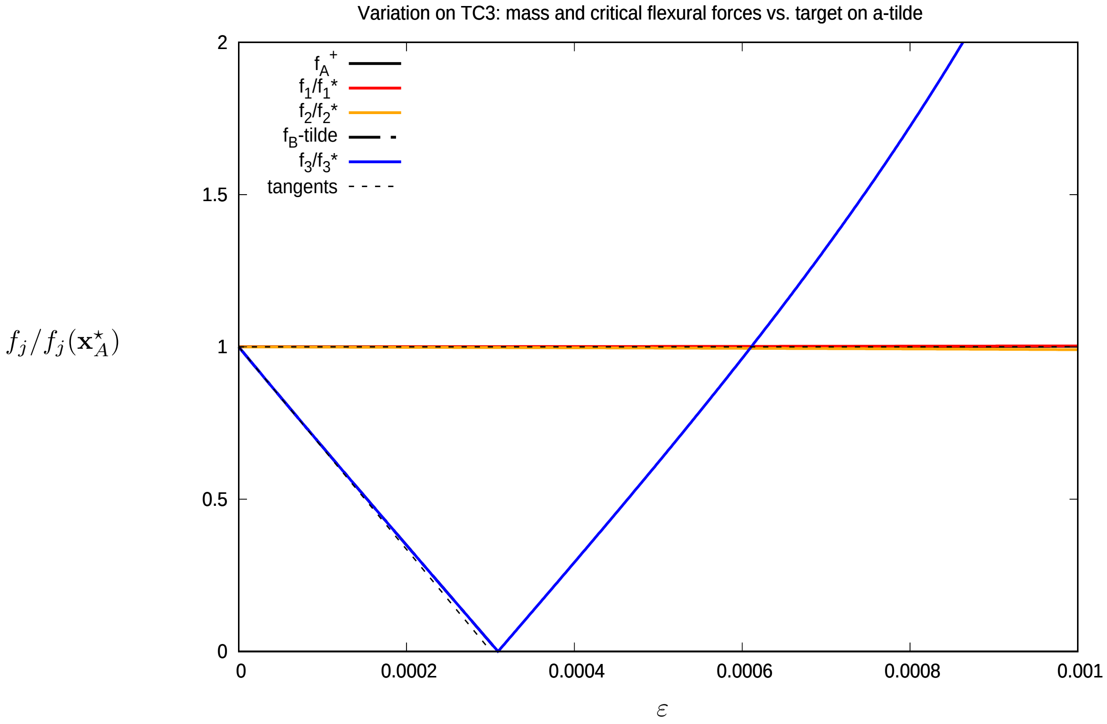

Figure 26: Test-case TC$_3$: Targeting the condition $f_1 = f_1(\mathbf{x}_{\tilde{a}})$ by a branch of continuum initiated at $\mathbf{x} = \mathbf{x}_a$ ($f_3 = |f_1(\mathbf{x}) - f_1(\mathbf{x}_{\tilde{a}})|$)

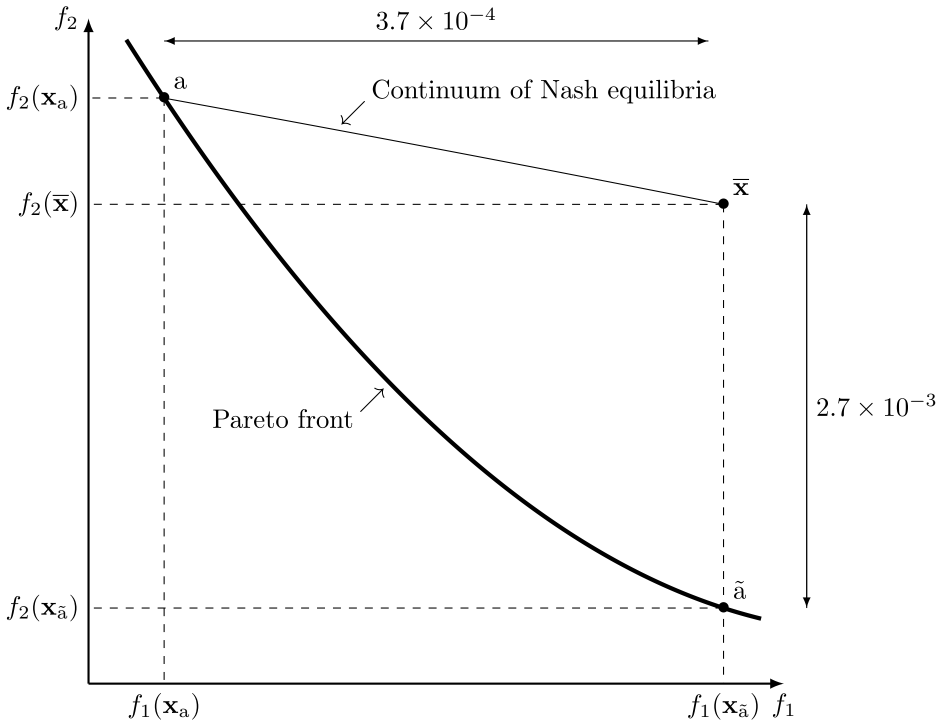

Figure 27: Approximate configuration of points a, ã and $\overline{\mathbf{x}}$; in this sketch, the arc of Pareto front is here simply represented by a parabolic fit through a and ã

```
testcase (character*80) :
Variation on TC3: mass and critical flexural forces vs. target on a-tilde

ndim
5

np
2

mfun
2

mtot
3

kc
1

xa_star
-1.5629544943845421
-1.2000870006928384
-0.83094529619039448
1.0769290088008954
0.34345599756029616

hfdiff
1.d-4

hbox
1.d-3

Bkappa
1.5d0

lstepmax
1000

eps1_over_epsmax
1.d-3

TOL
1.d-6

Lambdamax
10

mumax
5
```

Table 10: Parameter setting used to target $f_1 = f_1(\mathbf{x}_{\tilde{a}})$

References

[1] M. F. Ashby, A. G. Evans, N. A. Fleck, L. Gibson, J. Hutchinson, and H. Wadley, *Metal foams: a design guide*, Butterworth Heinemann, London, 2000.

[2] J.-A. Désidéri, *MGDA Software Platform for Multi-Objective Differentiable Optimization.* `http://mgda.inria.fr`.

[3] ——, *Quasi-Riemannian multiple gradient descent algorithm for constrained multiobjective differential optimization*, Research Report 9159, Inria, 21 March 2018. `https://hal.inria.fr/hal-01740075v1`.

[4] ——, *Platform for prioritized multi-objective optimization by metamodel-assisted Nash games*, Research Report 9290, Inria, September 2019. `https://hal.inria.fr/hal-02285197`.

[5] N. A. Fleck and V. S. Deshpande, *The resistance of clamped sandwich beams to shock loading*, Journal of Applied Mechanics, 71 (2004), pp. 386–401.

[6] L. J. Gibson and M. F. Ashby, *Cellular Solids : Structure and Properties*, Cambridge University Press, 1999.

[7] P. Leite, *Conception architecturale appliquée aux matériaux sandwichs pour propriétés multifonctionnelles*, PhD thesis, Université de Grenoble, École Doctorale I-MEP2, 2013. `http://www.theses.fr/2013GRENI053`.

[8] Q. Mercier, *Optimisation multicritère sous incertitudes : un algorithme de descente stochastique*, PhD thesis, Université Côte d'Azur, École Doctorale Sciences Fondamentales et Appliquées, 2018. `http://www.theses.fr/2018AZUR4076`.

[9] Q. Mercier, F. Poirion, and J.-A. Désidéri, *SMGDA : an uncertainty based multi-objective optimization approach. illustration to an airplane composite material*, Procedia Engineering, 199 (2017), pp. 1199–1203. `https://www.sciencedirect.com/science/article/pii/S1877705817337001`.

[10] ——, *Non-convex multiobjective optimization under uncertainty: a descent algorithm. application to sandwich plate design and reliability*, Engineering Optimization, 0 (2018), pp. 1–20.

[11] ——, *A stochastic multiple gradient descent algorithm*, European Journal of Operational Research, Elsevier Publish., 271 (2018), pp. 808–817.

[12] F. Poirion, Q. Mercier, and J.-A. Désidéri, *Descent algorithm for nonsmooth stochastic multiobjective optimization*, Computational Optimization and Applications, 68 (2017), pp. 317–331. `https://link.springer.com/article/10.1007/s10589-017-9921-x`.

[13] X. Qiu, V. S. Deshpande, and N. A. Fleck, *Finite element analysis of the dynamic response of clamped sandwich beam*, European Journal of Mechanics - A/Solids, 22 (2003), pp. 801–814.

Contents

RESEARCH CENTRE
SOPHIA ANTIPOLIS – MÉDITERRANÉE

2004 route des Lucioles - BP 93
06902 Sophia Antipolis Cedex

Publisher
Inria
Domaine de Voluceau - Rocquencourt
BP 105 - 78153 Le Chesnay Cedex
inria.fr

ISSN 0249-6399